Università degli Studi di Roma
"La Sapienza"

Dipartimento di Chimica

DOTTORATO DI RICERCA IN SCIENZE CHIMICHE
XXIII CICLO
ANNO ACCADEMICO: 2009 - 2010

Structural Investigation of Lanthanoid Coordination: a Combined XAS and Molecular Dynamics Study

Dottorando:
Andrea Zitolo

Relatore:
Prof.ssa Paola D'Angelo

Entia non sunt multiplicanda praeter necessitatem.
Guglielmo di Ockham

Contents

Chapter 1

Introduction

1.1 Ion hydration

Water is the most abundant compound on the surface of earth and, being the principal constituent of all living organism, it is the basis for life on our planet. Consequently, knowledge of the structural and dynamic properties of water is crucial in many problems of physics, chemistry and biology. Even if water has an apparently simple molecular structure, it is a rather complex fluid and shows many distinctive properties which are generally ascribed to the hydrogen bond at molecular level. The structure of water is in fact well described in terms of a dynamical network of hydrogen bonded clusters in which tetrahedral cages play a dominant role. The fundamental dynamical process occurring in water is the formation and breaking of hydrogen bonds which generally take place in the sub-picosecond time scale [1].

The structure and dynamics of these hydrogen bonded clusters is modified by changes of temperature and pressure, as well as by the introduction of solutes [2]. In particular, ions in solution strongly distort the structure of surrounding water molecules, as the result of the change in the microscopic balance of intermolecular forces, from that of water-water interactions in the neat solvent to that of ion-water interactions in the resulting solution. Our present understanding of the changes occurring to water in the presence of an ion is based on the scheme introduced by Frank and Wen [3] and Gurney [4] who considered three concentric solvent regions around the ions: the innermost region, the so called first hydration shell, in which the water molecules are strongly oriented by the ion and tend to be carried by the ion as it moves through the solution, the second hydration shell in which the water molecules are only weakly oriented by the ion and finally, in the outermost region far from the ion, the structure of water is generally the same as that of bulk water. Figure 1.1 provides a schematic picture of the hydration spheres of a metal cation having a first solvation shell of six water molecules. This is for example the situation encountered in many 3d metal ions.

Ions have been classified as structure makers and structure breakers according to their ability to induce structuring of water. Small ions with high electric charge are generally structure makers, as the water molecules in the

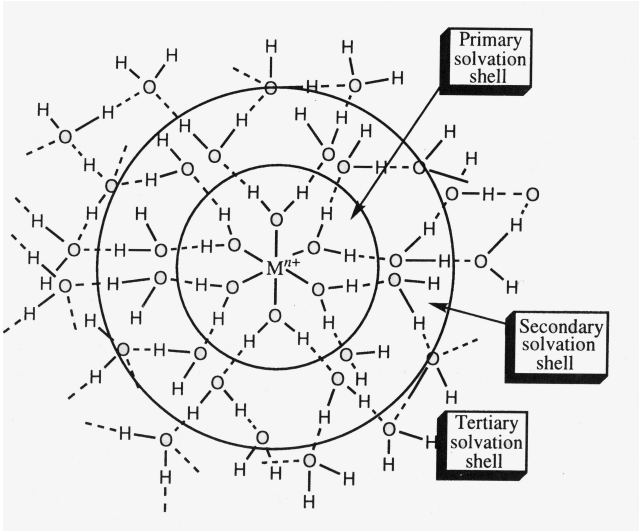

Figure 1.1: Structure of a generic hydrated metal cation in aqueous solution.

first solvation shell are strongly bound to the ion and it is appropriate to think of a well defined ion-water complex. Larger ions instead are often structure breakers as their main influence is the disruption of the hydrogen bond network characteristic of bulk water. All ions are hydrated to varying extents in water but the degree of hydration depends on a number of factor, such as the ionic size and the charge density [1]. Cations are more strongly hydrated in general than anions due to a combination of high positive charge density and a particularly strong interaction with the negatively polarized oxygen atom of water. However, a well defined first hydration shell of water molecules exists also around halide ions, even if the interaction (via the hydrogen atoms) is somewhat weaker [1].

The structural and dynamic properties of the hydration spheres of aqua ions are fundamental to understanding the behaviour of ions in chemical and biological systems and processes. Consequently, a large number of experimental techniques, primarily X-ray and neutron diffraction, have been applied to obtain structural information on the ion-water interaction. For 3d metal transition elements the identification of the primary hydration geometry, usually octahedral six-coordinated, has proved relatively straightforward [2]. For the rest of ions, including anions, alkaline and earth-alkaline cations, information on the hydration structure is not very conclusive, in principle as a result of the higher disordered environments and a general lack of direct information relating to static and dynamic properties of solvent molecules when they coordinate ions [2].

During the last several years it has been shown that X-ray absorption spectroscopy (XAS) is particularly well suited for the investigation of the local solvent structure of ions dissolved in water, due to its atomic selectivity and its sensitivity to dilute solutions. From the analysis of the Extended X-Ray Absorption Fine Structure (EXAFS) it is possible to obtain very accurate ion-

water first shell distances. However, in the case of disordered systems, such as ionic solutions, the uncertainty in the coordination numbers determined by the EXAFS analysis is usually too large for a conclusive determination of the geometry of hydration complexes. Conversely, a quantitative analysis of the X-ray Absorption Near Edge Structure (XANES) region, which includes the rising edge and about 200 eV above it, can provide accurate geometrical information on the hydration clusters existing in water. Nevertheless, the characterization of the structural and dynamical properties of ions and water molecules in the hydration spheres is very difficult to be obtained from experimental techniques only, and the combined use of experimental and theoretical methods is essential to obtain reliable information. Among computer simulation techniques, Molecular Dynamics is a powerful tool in the analysis of both static and dynamic properties of solvated ions in solution and has been extensively used in the last decades for the study of aqueous solutions [2].

In this context, the aim of this work is to unveil the detailed structure and dynamics in aqueous solutions of the lanthanoid(III) ions using a procedure which combines XAS spectroscopy and Molecular Dynamic simulation techniques.

1.2 Lanthanoids aqua ions

Recently, there has been growing interest in lanthanoids and their derivatives because of the emergence of novel application fields. A part from the well-known importance as contrast agents in magnetic resonance imaging techniques for medical diagnosis, there is a plethora of additional applications ranging from catalysis and organic synthesis, to nuclear waste management and liquid-liquid extraction from aqueous solutions [5]. Despite its importance, the fundamental understanding of the lanthanoid chemistry is still at an early stage of knowledge, as compared to 3d-transition metals. Lanthanoid cations belong to a chemical series whose hydration properties are of particular interest for both fundamental and applicative reasons, and questions about the change of structure of the first shell polyhedron across the series are still at the center of recent research works.

Within the lanthanoid series of fifteen chemically similar elements, including lanthanum, systematic changes occur of their chemical properties. At an early stage they were divided into two subgroups, the light and the heavy lanthanoids [6]. However, the point of division varied depending on the chosen property and was somewhat indefinite until Spedding and coworkers some 40 years ago introduced the concept of the so-called “gadolinium break”, based on a proposed change in the coordination number of the hydrated lanthanoid(III) ions in aqueous solution in the middle of the lanthanoid series. This proposal could be coupled to the electronic structure of these trivalent ions and the effects expected of the half-filled 4f shell. The proposal of Spedding and coworkers was based on changes in a number of physical chemical properties, such as partial molar volume [7], heat capacity [8], molar entropy

[8] and viscosity [9] around samarium, europium and gadolinium. The partial molar volumes should decrease continuously if the hydrated lanthanoid(III) ions have the same hydration structure taking the lanthanoid contraction into account. However, there is a discontinuity and an increase in the partial molar volumes from samarium to gadolinium, rationalized by a decrease in the hydration number of the heavier lanthanoid(III) ions. The light hydrated lanthanoid(III) ions in aqueous solution are shown to be nine-coordinated in tricapped trigonal prismatic (TTP) configuration, while the heavy ones are believed to have a square antiprismatic (SAP) configuration [10, 11, 12].

X-ray diffraction [13] and neutron scattering [14, 11] have been extensively used in the past to gain structural information on lanthanoid complexes both in solid state and in solution. Recently, a thorough analysis of new EXAFS data has shown that all of the lanthanoid(III) hydration complexes in aqueous solution retain a tricapped trigonal prism geometry, in which the bonding of the capping water molecules varies along the series [15]. In particular,the capping water molecules are equidistant for the largest lanthanoid(III) ions (La-Nd). Starting at samarium, distortion from regular symmetry becomes evident, with one of the capping water molecules more strongly bound to the Ln(III) ion. For the smallest Ln(III) ions (Ho-Lu), one of the capping water molecules is so strongly bound to the ion, as compared with the other two capping water molecules, that the occupancy of these two sites starts to decrease. As a result, the structure of the hydrated lutetium(III) ion can be described as a distorted tricapped trigonal prism with six water molecules in the prismatic positions having the same Lu-O bond length, and on average 2.2 water molecules in the capping positions with one Lu-O distance significantly shorter than the others [15].

From a computational point of view, Molecular Dynamics (MD) simulations, using classical, ab initio, or mixed quantum/classical interaction potentials have been used to determine structural and dynamical properties of lanthanoid(III) ions [5, 16, 17, 18, 19, 20, 21, 22, 23, 24, 25, 26, 27, 28, 29, 30]. Even if the determination of the coordination geometry of lanthanoid(III) ions is quite straightforward for crystalline samples with high symmetry [31, 32, 33] the characterization of structures in solutions and in solids where the lanthanoid(III) ions display water deficit is more elusive and very difficult to be obtained from the standard experimental techniques [15].

1.3 Aim of this work

In this work a detailed investigation of the structure and dynamics of lanthanoid(III) ions both in aqueous solution and in the solid state will be carried out combining X-ray absorption spectroscopy and Molecular Dynamics simulations. To this end we will apply a XANES fitting procedure, named MXAN (Minuit XANes) [34], to the analysis of both the K-edge and L_3-edge spectra of some Ln(III) ions in aqueous solution and to isostructural solid aqualanthanoid(III) trifluoromethanesulfonates $[Ln(H_2O)_n](CF_3SO_3)_3$. Although the quantitative XANES analysis has been successfully applied to

the study of several transition-metal ions in aqueous solution, allowing a quantitative extraction of the relevant geometrical information about the absorbing site [35, 36, 37, 38, 39, 40] understanding and interpreting the X-ray edge features of lanthanoids is still a methodological and theoretical challenge. In the past the lanthanoid L_3-edge X-ray absorption spectra have been most frequently used because the energy range involved (from 5 to 10 keV) is more accessible from standard synchrotron radiation sources. Moreover, the K-edges of lanthanoids cover the energy range 39 (La) to 63 (Lu) keV and because of the very short lifetime of the excited atomic state, the structural oscillations can be strongly damped. Nevertheless, a recent investigation on hydrated lanthanoid(III) ions both in aqueous solution and in solid trifluoromethanesulfonate salts has shown that the large widths of the core hole states do not appreciably reduce the potential structural information of the lanthanoid K-edge spectra [41]. In particular, because of the much wider k-range available, and the absence of double electron transitions, more accurate structural parameters are obtained from the analysis of K-edge than from the L_3-edge EXAFS data.

We will start the study with a detailed description of the XANES analysis only for three ions, neodymium(III), gadolinium(III), and lutetium(III), because they are representative of the structural changes relating to the first hydration shell along the series. For these three ions we will investigate the first coordination shell basing on a rigid model and then using the microscopic description derived from MD simulations to show the the potential of XANES spectroscopy in the structural investigation of poorly ordered systems. Subsequently we will extend the study on the coordination of other lanthanoid(III) ions in aqueous solution using a combined approach of EXAFS, XANES and Molecular Dynamics simulations techniques in order to give dynamics and structure information on the first hydration shell and on the second hydration shell too.

This thesis is organized as follows. Chapter 2 and 3 describe the basic concepts of X-ray absorption spectroscopy, the methods employed in the EXAFS and XANES data analysis, with particular emphasis on their application to the study of disordered systems, and the theoretical background of Molecular Dynamics simulations. The theoretical and experimental methods employed in the study of lanthanoids aqua ions are summarized in chapter 4. Chapter 5 describes the XANES results on the hydration properties of Nd(III), Gd(III), Yb(III) and Lu(III) from a static point of view, while chapter 6 describes the structural and dynamic properties of Nd(III), Gd(III) and Yb(III) using a combined XAFS and molecular dynamic approach. In chapter 7 is shown the potentiality of a combined EXAFS and polarized molecular dynamic study on all the lanthanoid series. Finally, chapter 8 summarizes and concludes this thesis.

Chapter 2

X-ray absorption spectroscopy

2.1 Introduction

X-ray absorption spectroscopy (XAS) measures the X-ray absorption coefficient, $\mu(E)$, as a function of the X-ray energy of the incident photon, $E = \hbar\omega$ (measured in eV). A XAS spectrum, in which the absorption coefficient is plotted as a function of E, shows an overall decrease of the X-ray absorption with increasing energy, with the exception of very sharp peaks at certain energies (called edges) due to the transitions of core electrons to high energy states (see Figure 2.1). The energies of these peaks correspond to the ionization energies of the core electrons. Each absorption edge is related to a specific atom present in the material and, more specifically, to a quantum-mechanical transition that excites a particular atomic core electron to the free or unoccupied continuum levels. The nomenclature for X-ray absorption reflects the origin of the core electron (see Figure 2.2). K edge refers to the transition that excites the innermost $1s$ electron, L_1 edge is due to the excitation of the $2s$ electron, while L_2 and L_3 edges are related to the excitations of the $2p$ electrons with electronic states $^2P_{1/2}$ and $^2P_{3/2}$, respectively. The transitions are always to unoccupied states with the photoelectron above the Fermi energy, which leaves behind a core hole. The energies of the edges are unique to the type of atom that absorbs in the X-ray and thus themselves are signatures of the atomic species present in a material.

From what has been said, it is clear that XAS, being an atomic probe, places few constraints on the samples that can be studied. All atoms have core level electrons, and XAS spectra can be measured for essentially every element on the periodic table. Moreover, crystallinity is not required for XAS measurements (even if it is also possible to measure XAS spectra of crystalline samples), making it one of the few structural probes available for noncrystalline and highly disordered materials, including solutions, amorphous solids and fluid samples in general. In many cases, XAS measurements can be made on elements of minority and even trace abundance, giving a unique and direct measurement of chemical and physical state of dilute species in a variety of systems. XAS spectra are recorded using the properties of synchrotron radiation, which provides tunable X-ray beams with high brilliance. In this way

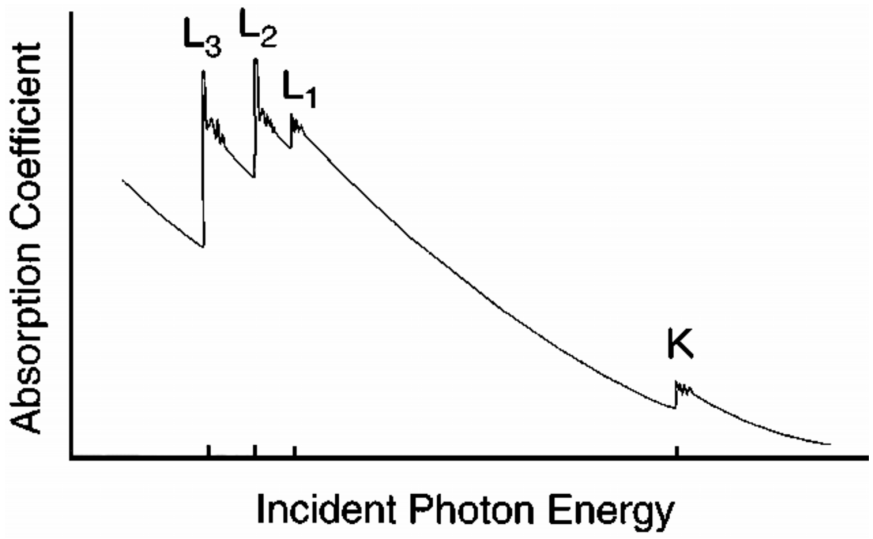

Figure 2.1: Typical XAS spectrum showing the K, L_1, L_2 and L_3 absorption edges.

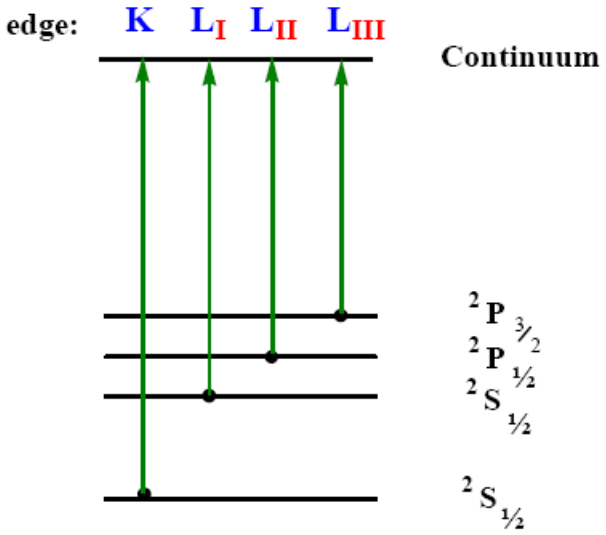

Figure 2.2: Schematic representation of the transitions that take place at the various absorption edges.

it is possible to obtain spectra with a very high signal/noise ratio.

A typical XAS spectrum is shown in Figure 2.1. When the energy of the incident photon, E, is greater than the ionization potential, E_0, of a given electron, this electron is emitted by the photoabsorber atom with a kinetic energy equal to the difference $E - E_0$ and undergoes a scattering process on the nearest atoms. This phenomenon produces a series of wiggles or oscillatory structures above the edge that modulate the absorption, typically by a few percent of the overall absorption cross section. These features contain detailed structural information on the atoms around the photoabsorber, such as interatomic distances and coordination numbers. However, it is important to stress that the information on bond angles and distances that can be obtained from a XAS spectrum is limited in a range of 4-5 Å from the photoabsorber atom [42]. The short-range character of XAS is due to the limited *mean free path* of the photoelectron and to the excited state lifetime (*core hole lifetime*). In fact the high-energy excited photoelectron state is not long lived, but must decay as a function of time and distance and thus cannot probe long-range effects. This decay is due primarily to inelastic losses (i.e. "extrinsic losses") as the photoelectron traverses the sample, either by interacting with and exciting other electrons, or by creating collective excitations (plasmon production). In addition, the intrinsic lifetime of the core-hole state ("intrinsic losses") has to be clearly considered [42]. The net effect is that XAS can only measure the local atomic structure over a range limited by the net lifetime of the excited photoelectron. In this sense, XAS is very different from other techniques such as X-ray diffraction or neutron diffraction, in which also long-range interactions provide a detectable contribution to the experimental spectrum.

A XAS spectrum is conventionally divided into two regions: the X-ray Absorption Near Edge Structure (XANES) up to about 50 eV beyond the absorption edge, and the Extended X-ray Absorption Fine Structure (EXAFS) at higher energies. The border between XANES and EXAFS regions is shown in Figure 2.3. The division of a XAS spectrum is only formal and it is due to the different theoretical treatment and approximations used to calculate the absorption cross section in the two regions. In both cases, a full quantum description of the X-ray absorption phenomenon is not possible, and, as a consequence, approximate models have to be employed. In these models the emitted electron is treated as a quasi-particle (photoelectron) that moves in an effective potential which takes into account both the interaction with the other electrons of the photoabsorber atom and the potential generated by the surrounding atoms. However, as the energy of the photoelectron increases, further approximations can be made to obtain a simpler data analysis protocol. For this reason, historically the first quantitative analyses were made on the high energy part of the absorption spectrum (EXAFS) while the XANES spectra have been analyzed for many years only on a qualitative way.

XAS phenomenon was discovered around 1930 but only 40 years later became a structural investigation technique, following the incoming of better X-ray sources in the experiments and the development of theories able to

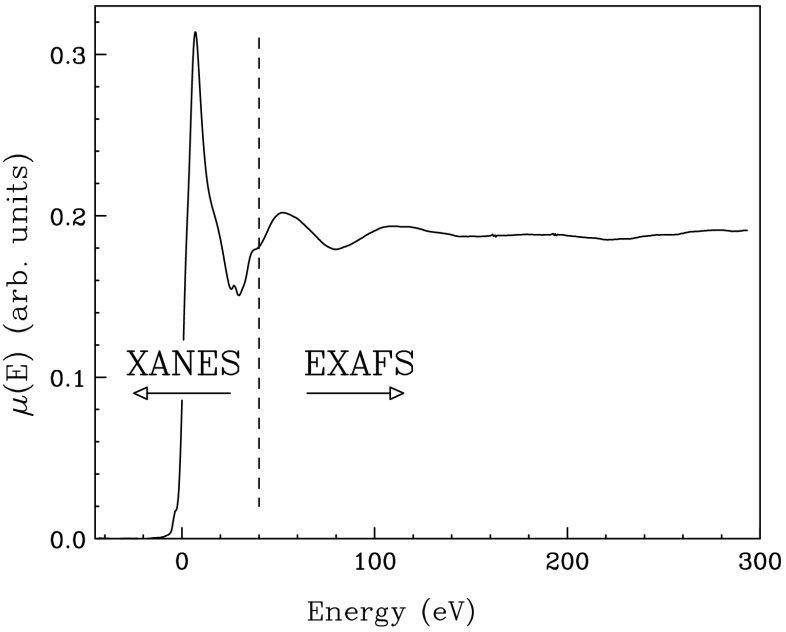

Figure 2.3: Division of the absorption spectrum between XANES and EXAFS regions.

provide a quantitative interpretation of experimental data. The first works were published by Sayers et al. in 1971 and 1975 [43, 44]; in these works a semi-empiric parameterization of the EXAFS signal is proposed for the first time. Later, the work of different groups lead to the development of theories able to explain the many physical phenomena involved in radiation absorption, confirming the validity of Sayers' approach.

Some years ago a unifying scheme of interpretation of the X-ray absorption spectra, based on the Multiple Scattering (MS) theory and valid for the whole energy range, has been developed [45]. An important result of this MS approach, which is based on the Green's function formalism, is that the expression for the absorption cross section ($\sigma(E)$) can be factored in an atomic term ($\sigma_0^l(E)$) depending only on atomic electronic properties, and in a structure factor ($\chi^l(E)$) containing all the structural information on the environment:

$$\sigma(E) \propto \sigma_0^l(E)\chi^l(E) \tag{2.1}$$

The expression for $\chi^l(E)$ obtained within the MS theory is given by [46]:

$$\chi^l(E) = \frac{1}{(2l+1)sin^2\delta_l^0} \sum_m Im[(I + T_a G)^{-1} T_a]_{lm,lm}^{00} \tag{2.2}$$

where I is the unit matrix, G is the matrix describing the spherical wave propagation of the photoelectron from one site to another around the photoabsorber, T is the diagonal matrix describing the scattering process of the photoelectron by the atoms located at the various sites around the photoabsorber and δ_l^0 is the phase shift of the photoabsorbing atom (located at site

0) for angular momentum l. Therefore, the fundamental problem in XAS calculations is the inversion of the matrix reported in equation 2.2. In the high energy region, this problem can be overcome by expanding the matrix inverse in a series in which each term corresponds to the contribution of a scattering path, or in other words, the matrix inverse can be written as a sum over all of the multiple scattering paths [46]. This is possible because in the high energy regime the series is convergent. Conversely, in the XANES region the series does not converge, and the structure factor has to be calculated by the exact matrix inversion. This is one of the most fundamental differences between the theoretical approaches used in the EXAFS and XANES regions of the spectrum. The physical reason of this difference is that in the XANES regime the electron kinetic energy is small and the scattering on the neighbouring atoms tends to be strong, while the effect of the scatterers becomes smaller at higher energies and the photoelectron is only weakly scattered.

In this framework, several data analysis programs have been developed to analyze the experimental data. In these codes two fundamental approximations are generally used. The first one is the so called muffin-tin approximation, in which the potential generated by the atoms surrounding the photoabsorber is spherically averaged inside muffin-tin spheres around each atom, and averaged to a constant in the interstitial region (delimited by a convenient outer sphere enclosing the cluster used in the calculations). The second approximation concerns the choice of the effective optical potential in which the photoelectron moves. The most used approximation is the complex Hedin-Lundqvist energy dependent potential whose imaginary part accounts for extrinsic losses [47]. While this approach is a good approximation in the EXAFS region, in the low-energy regime the complex part of the Hedin-Lundqvist potential introduces an excessive loss in the transition amplitude of the primary channel and thus other approximations are exploited, as we shall see in section 2.3.

In the remainder of this chapter a brief introduction to the techniques used in the EXAFS and XANES data analysis will be given, with particular emphasis on their application to the study of disordered systems.

2.2 EXAFS analysis

The fundamental quantities used in the analysis of EXAFS spectra are defined as follows:

- $\mu(E)$ is the atomic absorption coefficient, defined as the attenuation of the X-ray beam per distance unit, which is proportional to the absorption cross section.

- $\mu_0(E)$ is the absorption coefficient of the isolated atom.

- $k = \frac{p}{\hbar} = \sqrt{\frac{2m_e}{\hbar^2}(E - E_0)}$ is the photoelectron wave number.

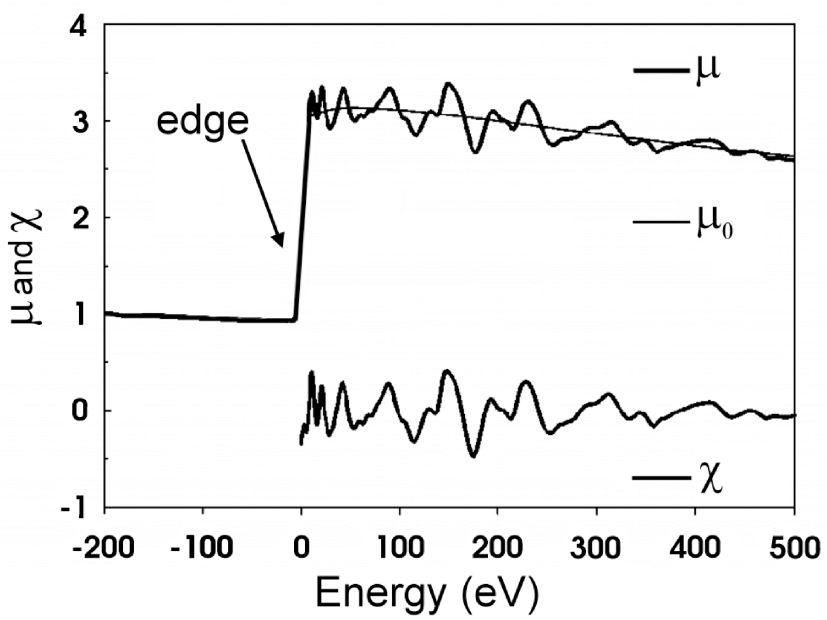

Figure 2.4: Relation between $\mu(E)$, $\mu_0(E)$ and $\chi(E)$.

- $\chi(k) = \frac{\mu - \mu_0}{\mu_0}$ is the normalized oscillating part of the spectrum, which is obtained by eliminating the absorption of the isolated atom from the signal and normalizing it to unity.

The relation between these quantities is shown in figure 2.4. $\chi(k)$ contains all the structural information on the system in an analogous way to the structure factor $S(q)$ in diffraction techniques.

Sayers et al. developed a quantitative parameterization of $\chi(k)$ which has become the standard for current EXAFS analysis and it is given by [43]:

$$\chi(k) = S_0^2 \sum_i N_i \frac{f_i(k)}{kR_i^2} \sin(2kR_i + 2\delta_c(k) + \phi_i(k)) e^{-\frac{2R_i}{\lambda(k)}} e^{-2\sigma_i^2 k^2} \tag{2.3}$$

where S_0^2 is a phase reduction factor, the index i is related to the N_i equivalent scattering atoms at distance R_i from the photoabsorber, $\delta_c(k)$ and $\phi_i(k)$ are the phase displacements due to the photoabsorber atom and to the scatterers, respectively. σ_i is the average square fluctuation of the bond distances (or Debye-Waller factor) and contains the structural disorder, and f_i is the diffusion amplitude. The substantial validity of this expression is due to the above mentioned fact that in the high energy range the contributions of the different scattering paths can be factorized and for the special case in which only two-body paths are accounted for, the functional form of equation 2.3 is recovered.

The Debye-Waller factor in equation 2.3 accounts for the fact that, due to the thermal vibrations, the atomic positions oscillate and thus R_i is only the average value of a distance distribution. For low enough temperatures, i.e. in the harmonic approximation limit, this distribution is well approx-

imated by a Gaussian function of width proportional to the Debye-Waller factor (this is the origin of the $e^{-2\sigma_i k^2}$ term in equation 2.3). The analysis of crystalline samples is usually made describing the coordination around the photoabsorber atom using these Gaussian shells. On the other hand, at elevated temperatures or in disordered systems, such as aqueous ionic solutions, the distribution functions become broad and asymmetric towards the large distances, the harmonic approximation is no longer valid and the appropriate description of these systems can be performed in terms of radial distribution functions ($g(r)$). When an asymmetric distribution is present the first peak of the radial distribution functions can be modeled using a set of Gamma functions. These functions are described by an average distance R, a coordination number (N_c), a standard deviation σ, and an asymmetry factor (skewness) $\beta = 2p^{\frac{1}{2}}$. Their general expression is given by:

$$f(r) = N_c \frac{p^{\frac{1}{2}}}{\sigma\Gamma(p)} \left[p + \frac{r-R}{\sigma} p^{\frac{1}{2}} \right]^{(p-1)} e^{-\left[p + \frac{r-R}{\sigma} p^{\frac{1}{2}}\right]} \tag{2.4}$$

where $\Gamma(p)$ is the Euler Gamma function associated to the parameter p.

The EXAFS spectroscopy is particularly suited to the study of the local environment around a photoabsorber atom, such as an ion in aqueous solution, since the EXAFS signal depends only on the distribution functions related to photoabsorber atom; this is one of its main advantages over diffraction techniques where the structure factor $S(q)$ is the superimposition of the $N(N+1)/2$ different distribution functions associated to the N atoms of the systems, and it is very difficult to isolate single contributions. Therefore, in systems like ionic solutions the greater contribution to the structure factor is from bulk water and diffraction techniques can be employed only in rather concentrated solutions (1-2 M), while EXAFS can be used at very low concentrations. Moreover, EXAFS provides values of bond distances with very high accuracy, typically of the order of 0.01 Å, about one order of magnitude greater than the majority of diffraction techniques. On the other hand, EXAFS can only give short range (up to 4-5 Å) information, as it has been already discussed in the previous section, and, in the case of disordered systems, the fitting parameters are often correlated and the EXAFS data analysis can lead to ambiguous result. A strategy to help in the extraction of the structural details contained in the EXAFS spectra of disordered systems is to include independent information derived from computer simulations. In particular, in recent years it has been shown that EXAFS data analysis of ions and molecules in solution can derive strong benefit by using the radial distribution functions calculated from Molecular Dynamics simulations as starting models. In this case the theoretical signal $\chi(k)$, associated for example to the ion-oxygen distribution in an aqueous ionic solution, is expressed as a function of the ion-oxygen $g(r)$ calculated from the Molecular Dynamics trajectories:

$$\chi(k) = \int_0^\infty dr 4\pi r^2 \rho g(r) A(k,r) \sin(2kr + \phi(k,r)) \tag{2.5}$$

where $A(k,r)$ and $\phi(k,r)$ are amplitude and phase functions and ρ is the density of scattering atoms. With such a procedure, it is possible to analyze the EXAFS data using a realistic structural model and including the contribution of the second hydration shell.

The theoretical signal is then compared with the experimental one by minimizing the following function:

$$R_i(\{\lambda\}) = \sum_{i=1}^{N} \frac{[\alpha_{exp}(E_i) - \alpha_{mod}(E_i; \lambda_1 \dots \lambda_p)]^2}{\sigma_i^2} \tag{2.6}$$

where N is the number of experimental points E_i, $\{\lambda_i\}$ is the set of p parameters that are optimized and σ_i^2 is the variance associated to each experimental datum $\alpha_{exp}(E_i)$. On the basis of the final value of $R_i(\{\lambda\})$ and of the agreement between the experimental and theoretical spectra, the correctness of the starting $g(r)$ can be evaluated. Therefore, this combined EXAFS-Molecular Dynamics approach on the one hand allows one to verify the reliability of the Molecular Dynamics simulations by comparing the theoretical results with the experimental data, on the other hand provides a useful starting model in the EXAFS analysis of disordered systems. The structural parameters of the starting model can be fitted in order to obtain the better possible agreement with the experimental data, and an accurate description of the first coordination shell can thus be obtained.

It is important to stress that besides the radial (two-body) distribution functions, also information on three-body, four-body ... distribution functions can be obtained from the EXAFS analysis, that are calculated by means of the MS theory as implemented in the GNXAS software package [48]. Obviously, this is possible only when MS processes provide a detectable contribution to the EXAFS experimental spectrum.

2.3 XANES analysis

The XANES region of the spectrum is extremely sensitive to the geometric environment of the absorbing atom and, in principle, an almost complete recovery of the three-dimensional structure can be achieved from it. The possibility to gain structural information from the XANES spectra is extremely important for dilute and biological systems where the low signal-to-noise ratio of the experimental data hampers a reliable analysis of the EXAFS region. Moreover, in the study of disordered systems coordination numbers cannot be accurately determined from the EXAFS data due to their large correlation with the Debye-Waller factors, and for these systems the analysis of the XANES region can thus be essential to address some of the shortcomings of EXAFS. However, the analysis of the low-energy part is much more difficult to be performed due to the theoretical approximation in the treatment of the potential [49] and requires the use of heavy time-consuming algorithms [50] to calculate the absorption cross section in the framework of the full MS approach. For this reason, this technique has been for a long time used as a

qualitative method used as a help for standard EXAFS studies [51] and only some years ago some methods have been proposed in the literature which performs a quantitative analysis of XANES [52]. In particular a new software procedure, named MXAN, has been developed [34]. This method is based on the comparison between the XANES experimental spectrum and several theoretical calculations performed by varying selected structural parameters associated with a given starting model. Starting from a putative geometrical configuration around the photoabsorber atom, the MXAN package is able to reach the best-fit conditions in a reasonable time, by minimizing a residual function R_{sq} in the space of the structural and non-structural parameters defined as:

$$R_{sq} = n \frac{\sum_{i=1}^{m} w_i \left[(y_i^{\mathrm{th}} - y_i^{\mathrm{exp}}) \varepsilon_i^{-1} \right]^2}{\sum_{i=1}^{m} w_i} \tag{2.7}$$

where n is the number of independent parameters, m is the number of experimental points, y_i^{th} and y_i^{exp} are the theoretical and experimental values of the cross section, ε_i is the error on each experimental point and w_i the statistical weights. The X-ray absorption cross section is calculated using the full MS scheme within the muffin-tin approximation for the shape of the potential. The exchange and correlation part of the potential are determined on the basis of the local density approximation of the self-energy of the photoelectron using an appropriate complex optical potential. The real part of the self-energy is calculated either by the Hedin-Lundqvist energy-dependent potential or by the X_α approximation. However, to avoid over-damping at low energies due to the complex part of the Hedin-Lundqvist potential, the MXAN method can account for all inelastic processes by convolution with a broadening Lorentzian function having an energy-dependent width $\Gamma_{\mathrm{tot}}(E)$ of the form [34]:

$$\Gamma_{\mathrm{tot}}(E) = \Gamma_c + \Gamma_{\mathrm{mfp}}(E) \tag{2.8}$$

The constant part Γ_c accounts for both the experimental resolution and the core-hole lifetime, while the energy dependent term $\Gamma_{\mathrm{mfp}}(E)$ represents all the intrinsic and extrinsic inelastic processes. The $\Gamma_{\mathrm{mfp}}(E)$ is zero below an energy onset E_s (which, in extended systems, correspond to the plasmon excitation energy), and starts increasing from a given value A, following the universal form of the mean free path in solids [53].

The MXAN procedure has been successfully applied to the study of several systems, both in the solid and liquid state, allowing a quantitative extraction of the relevant geometrical information about the absorbing site [54, 35, 56]. However, in the case of ionic solutions the XANES spectra have been usually computed reducing the system to a single structure since the contribution from molecules and arrangements instantaneously distorted cannot be calculated using the analysis standard methods. A promising strategy to overcome this problem is to analyze the XANES spectra using the microscopic dynamical description of the system derived from Molecular Dynamics simulations. In this framework, we have developed a computational procedure which uses MXAN and Molecular Dynamics simulations to generate a configurational av-

eraged XANES spectrum and we have applied it to the study of ionic aqueous solutions.

Chapter 3

Molecular Dynamics Simulations

Molecular Dynamics, strictly speaking, is the simultaneous motion of atomic nuclei and electrons forming molecular entities. A complete description of such a system requires in principle solving the full time-dependent Schrödinger equation including both electronic and nuclear degrees of freedom. This is however a too much expensive computational task which is in practice unfeasible for systems consisting of more than three atoms. In order to study the dynamics of the vast majority of chemical systems several approximations have therefore to be introduced. First of all, it is assumed in Molecular Dynamics with the Born-Oppenheimer approximation that the motion of electrons and nuclei is separable, and the electron cloud adjusts instantaneously to changes in the nuclear configuration. As a consequence, nuclear motion evolves on a PES, associated with the electronic quantum state which is obtained by solving the time-independent electronic Schrödinger equation for a series of fixed nuclear geometries. In practice, most Molecular Dynamics simulations are performed on the ground state PES.

Moreover, in addition to making the Born-Oppenheimer approximation, Molecular Dynamics treats the atomic nuclei as classical particles whose trajectories are computed using the laws of classical mechanics. This is a very good approximation for molecular systems as long as the properties studied are not related to the motion of light atoms (like the hydrogen atoms, which show quantum mechanical behaviour in certain situations such as tunneling phenomena) or vibrations with frequency ν such that $h\nu > k_B T$.

The potential functions which describe the intermolecular and intramolecular interactions between classical nuclei can be treated at various levels of approximation. In classical Molecular Dynamics the interaction potential is expressed as a simple sum of pair potentials. On the other hand, ab initio Molecular Dynamics computes interactions at a much more fundamental level using electronic structure methods. In the mixed Quantum Mechanical and Molecular Mechanics (QM/MM) methods instead the "important" part of the system, for instance where a chemical reaction is taking place, is treated with electronic structure calculations whereas the rest of the system

is described by a classical force field. In this chapter an introduction to the classical Molecular Dynamics is given, followed by a brief description of the polarization in molecular simulation.

3.1 Classical Molecular Dynamics

In the classical Molecular Dynamics simulations the time evolution of a system composed by M particles (generally atoms) is obtained by solving the Newton's equation of motion step-by-step [59]:

$$M_a \ddot{\mathbf{R}}_a = \mathbf{F}_a \quad a = 1, 2, \ldots, M \tag{3.1}$$

where M_a and $\mathbf{R}_a$ are the mass and the position of particle a and $\mathbf{F}_a$ is the force acting on particle a given by:

$$\mathbf{F_a} = -\frac{\partial V}{\partial \mathbf{R_a}} \tag{3.2}$$

V is a potential energy function which depends on the complete set of $3M$ particle coordinates. In classical Molecular Dynamics the complex potential energy function is represented by a sum of simple functions, called force fields. In these force fields, the interactions are usually divided into bonded and non-bonded [60]:

$$V = V_{bonded} + V_{non-bonded} \tag{3.3}$$

Bonded interactions are written as a sum of various terms:

$$V_{bonded} = V_{bonds} + V_{angles} + V_{dihedrals} + V_{impr-dihedr} \tag{3.4}$$

V_{bonds} describes the stretching between the atoms in the system covalently bonded:

$$V_{bonds} = \sum_{bonds} \frac{1}{2} k_{b_{ij}} (b_{ij} - b_{ij}^0)^2 \tag{3.5}$$

where the covalent bond between atoms i and j is represented by a harmonic potential with force constant k_{bij}, instantaneous distance b_{ij} and equilibrium distance b_{ij}^0. For some systems that require an anharmonic bond stretching potential, other functional forms can be used such as the Morse potential [61]. V_{angles} describes the bond angle vibrations:

$$V_{angles} = \sum_{angles} \frac{1}{2} k_{\theta_{ijk}} (\theta_{ijk} - \theta_{ijk}^0)^2 \tag{3.6}$$

where the bending of the bond angle between a triplets of atoms i, j and k is modeled by a harmonic potential with force constant $k_{\theta_{ijk}}$, instantaneous angle θ_{ijk} and equilibrium angle θ_{ijk}^0. $V_{dihedrals}$ mimics the vibrations of dihedral

angle (four-body) interactions and is generally modeled as:

$$V_{dihedrals} = \sum_{dihedrals} \frac{1}{2} k_{\phi_{ijkl}} [1 + \cos(n\phi_{ijkl} - \gamma)] \tag{3.7}$$

where ϕ_{ijkl} is the angle between the ijk and jkl planes. $V_{impr-dihedr}$ represents a special type of dihedral interaction (called improper dihedral) which is used to force atoms to remain in a plane or to prevent transitions to a configuration of opposite chirality (a mirror image) and, in harmonic approximation, is given by:

$$V_{impr-dihedr} = \sum_{impr-dihedr} \frac{1}{2} k_{\xi_{ijkl}} (\xi_{ijkl} - \xi^0_{ijkl})^2 \tag{3.8}$$

where $k_{\xi_{ijkl}}$, ξ_{ijkl} and ξ^0_{ijkl} are the force constant, instantaneous and equilibrium improper dihedral angle, respectively.

As far as the non-bonded interactions are concerned, atoms are represented by charged point particles interacting with each other by parameterized model potentials. One of the most used functional form of $V_{non-bonded}$ is given as:

$$V_{non-bonded} = \sum_{pairs(ij)} \left(\frac{1}{4\pi\epsilon_0} \frac{q_i q_j}{\epsilon_r R_{ij}}\right) + \sum_{pairs(ij)} \left(\frac{C^{(12)}_{ij}}{R^{12}_{ij}} - \frac{C^{(6)}_{ij}}{R^6_{ij}}\right) \tag{3.9}$$

where the first term describes the Coulomb interactions between all of the atomic partial charges of the system (q_i and q_j are the partial charges of particles i and j placed at a distance R_{ij}), while the second term represents the van der Waals interactions by means of a Lennard-Jones potential which is the most commonly used form.

Aspects and details of the Molecular Dynamics simulation techniques will not be discussed here for the sake of brevity. However, it is noteworthy to summarize just a few points:

- The Newton's equations of motion 3.1 are integrated numerically step-by-step. Many algorithms have been designed to do this which are generally based on a Taylor expansion of the particle positions around the positions at a certain time instant. Among these methods, the most commonly used are the Verlet [62] and the leap-frog [63] algorithms. These two methods have the important property to be time-reversible, like the Newtonian equations of motion [64].

- Periodic boundary conditions [60] are applied in Molecular Dynamics simulations in order to minimize edge effects which may produce artifacts in a finite system. The atoms of the system to be simulated are put into a space-filling box, which is surrounded by translated copies of itself. There are thus no boundaries of the system. However, this imposed artificial periodicity by itself may cause errors, especially when considering properties which are influenced by long-range correlations.

- Long range non-bonded interactions are generally not calculated beyond a certain cutoff distance around each particle, in order to reduce the computational cost of the simulations. However, as far as the Coulomb interactions are concerned, the use of a simple cutoff can introduce serious artifacts and, for this reason, several techniques have been developed for handling long range interactions, the most popular of them being the Ewald summation [65] and the Particle Mesh Ewald methods [66, 67].

- Constraints are often used in Molecular Dynamics simulations, i.e. bonds are treated as being constrained to have fixed length. This is very useful when bonds have very high vibration frequencies and should be treated in a quantum mechanical way rather than in the classical approximation. Moreover, they allow to increase the integration time step and thus to perform longer simulations. The most commonly used constraints methods are the LINCS [68] and SHAKE [69] algorithms.

- When solving the Newton's equations of motion 3.1 the energy is a constant of motion and the simulation is performed in an *NVE* ensemble. However, it is often more convenient to carry out simulations in other ensembles, such as *NVT* or *NPT*. To this end, several approaches have been developed which control the temperature and the pressure of a system. As far as the temperature control is concerned, widely used techniques are the Berendsen [70] and Nosé-Hoover [71, 72] methods, while for the pressure control the Parrinello-Rahman scheme [73, 74] is extensively employed.

3.2 Accounting for polarization in molecular simulation

Polarization plays an important role in the energetics of molecular systems. Most computer simulation studies do not treat electronic polarizability explicitly, but only implicitly using effective charges, dielectric permittivities or continuum electrostatics methods. Yet, the introduction of explicit polarizability into molecular models and force fields is unavoidable when more accurate simulation results are to be obtained. If the polarization is not taken into account, the electrostatic energy V_{elec} corresponds to a pure Coulomb interaction:

$$V_{elec} = \frac{1}{2} \sum_{pairs(ij)} \left(\frac{q_i q_j}{r_{ij}}\right) \tag{3.10}$$

Various ways to account for polarizability in molecular simulation exist and one strategy consists in assigning isotropic polarizabilities and induced dipoles at each atomic site.In this framework the energy V_{elec} is composed of a charge-

charge interaction, charge-dipole and dipole-dipole energy:

$$V_{elec} = \frac{1}{2} \sum_{pairs(ij)} \left[\frac{q_i q_j}{r_{ij}} + \frac{1}{r_{ij}^3}(-q_i \mathbf{p}_j + q_j \mathbf{p}_i) \cdot \mathbf{r}_{ij} + \mathbf{p}_i \cdot \overline{\mathbf{T_{ij}}} \cdot \mathbf{p}_j \right] + \frac{1}{2} \sum_i \mathbf{p}_i \cdot \overline{\alpha_i}^{-1} \cdot \mathbf{p}_i \tag{3.11}$$

where, following Thole's induced dipole model [57] each atomic site i carries one permanent charge q_i and one induced dipole $\mathbf{p_i}$ associated with an isotropic atomic polarizability tensor $\overline{\alpha_i}$, $\mathbf{r_{ij}}$=$\mathbf{r_i}$ - $\mathbf{r_j}$:

$$\overline{\mathbf{T_{ij}}} = \frac{1}{r_{ij}^3}\left(\overline{1} - 3\frac{\mathbf{r}_{ii}\mathbf{r}_{ij}}{r_{ij}^2}\right) \tag{3.12}$$

and

$$\frac{1}{2} \sum_i \mathbf{p}_i \cdot \overline{\alpha_i}^{-1} \cdot \mathbf{p}_i \tag{3.13}$$

is the polarization energy.

Chapter 4

Methods employed in the study of lanthanoids aqua ions

4.1 X-ray absorption spectroscopy

4.1.1 X-ray absorption measurements

Aqueous solutions of the lanthanoid(III) ions (Ln(III)) were made by dissolving a weighed amount of hydrated trifluoromethanesulfonates salts $[Ln(H_2O)_n](CF_3SO_3)_3$ (in which Ln=Nd, Gd, Yb and Lu) in freshly distilled water. The concentration of the samples was 0.2 M and the solutions were acidified to about pH=1 by adding trifluoromethanesulforic acid to avoid hydrolysis. Solid $[Nd(H_2O)_9](CF_3SO_3)_3$, $[Gd(H_2O)_9](CF_3SO_3)_3$, $[Yb(H_2O)_{8.7}](CF_3SO_3)_3$ and $[Lu(H_2O)_{8.2}](CF_3SO_3)_3$ were diluted with boron nitride to give an absorption change over the edge of about one logarithmic unit. The K-edge spectra were collected at ESRF, on the bending magnet X-ray absorption spectroscopy beamline BM29 [75] in transmission geometry. The storage ring was operating in 16-bunch mode with a typical current of 80 mA after refill. The aqueous solutions were kept in cells with Kapton film windows and Teflon spacers ranging from 2 to 3 cm depending on the sample. The L_3-edge measurements were performed at the wiggler beamline 4-1 at the Stanford Synchrotron Radiation Laboratory (SSRL), Stanford, U.S.A., which was operated at 3.0 GeV and a maximum current of 100 mA. In this case simultaneous data collection was performed both in transmission and fluorescence mode. The stations at ESRF and SSRL were equipped with a Si[511] and Si[111] double-crystal monochromator, respectively. Higher order harmonics were reduced by detuning the second monochromator crystal to reflect, at the end of the scans, 80% of maximum intensity at the K-edge energies and 30-50% of maximum intensity at the L_3-edges, with the lower value at lower energy. Internal energy calibration was made when possible with a foil of the corresponding lanthanoid metal.

4.1.2 XANES data analysis

The quantitative XANES data analysis of the crystalline samples and the aqueous solution with a static model has been performed by means of the MXAN procedure which is described in section 2.3.

The K-edge XANES spectra of lanthanoid(III) ions are strongly affected by the short core-hole lifetime of the excited photoelectron (the core-hole widths at the K-edges are Γ=17.3, 22.3, 31.9 and 33.7 eV for Nd, Gd, Yb and Lu respectively [76]). As a consequence the edge resonance is strongly damped and the intensity of the main transition peaks becomes very small. Recently, core-hole width deconvolution methods have been developed [77] and applied to the analysis of the XANES spectra at the Hg L_3 and Cd K-edges [78, 36, 79]. This treatment largely facilitates the detection of spectral features and the comparison with theoretical calculations. Even if in principle the deconvolution procedure could introduce small distortions in the experimental data, the advantage of this approach is to avoid the use of the phenomenological broadening function in the calculation of the theoretical spectrum to mimic electronic damping. In the present case the Nd, Gd, Yb and Lu K-edge raw experimental data have been deconvolved of the whole tabulated core hole width and a Gaussian filter with full width at half-maximum of about 7.4, 8.0, 12.4 and 14 eV has been used, for Nd, Gd, Yb, and Lu respectively. The MXAN fitting procedure has been applied to lanthanoid(III) ions in hydrated trifluoromethanesulfonate crystals including either the first shell water molecules only or the first plus the second coordination shells. The hydrogen atoms were always included in the analyses. The cluster size and the l_{max} value (i.e., the maximum l-value of the spherical harmonic expansion of the scattering path operators) were chosen on the basis of a convergence criterion.

The XANES spectra of Ln(III) ions in aqueous solution have been analyzed starting from the microscopic description of the system derived from MD simulations. In the first step the XANES spectra associated with the MD trajectories have been calculated using only the real part of the HL potential. In this way the theoretical spectra do not account for any intrinsic and extrinsic inelastic process. In the second step a minimization in the non-structural parameter space has been carried out to perform a comparison with the experimental data. In particular, the inelastic processes are accounted for by convolution with the broadening Lorentzian function defined by equation 2.8. In the case of the K-edge XANES deconvolved spectra the constant part Γ_c, which accounts for the core-hole lifetime, has not been included in our calculations as it has been removed from the experimental data. For the L_3-edge spectra fixed Γ_c values of 4.60, 3.65, and 4.01 eV have been used for Yb, Nd, and Gd, respectively. In all cases the experimental resolution has been taken into account by convolution with a Gaussian function whose widths Γ_{exp} are reported in Table 6.2. For each ion two MD trajectories have been extracted from the total simulation, the former containing the first shell nonahydrated cluster only, the latter containing both the first and the second hydration shells. In particular, we have considered all the water molecules

separated from the ion by a distance shorter than 6.0 Å. From each trajectory we extracted 500 snapshots saved every 10 ps. Each snapshot has been used to generate the XANES spectrum associated with the corresponding instantaneous geometry, and the averaged theoretical spectrum has been obtained by summing all the spectra and dividing by the total number of MD snapshots used. The total sampling length that is necessary to have a statistically significant average has been determined performing, for each averaged theoretical spectrum, a statistical treatment of the data. In particular we have calculated a residual function defined by the equation 2.7. A residual value of 10^{-4} was chosen to establish the number of spectra which are necessary to have a statistically significant average. The results of this analysis are shown in Figure 4.1 for the L_3-edge of Yb(III) in water as an example. In this figure the RMS function is plotted against the number of averaged spectra for the first only and first plus second hydration shells. As evident from the plots a lower number of spectra is necessary in the former case, but in all cases 500 configurations are enough to reach convergence.

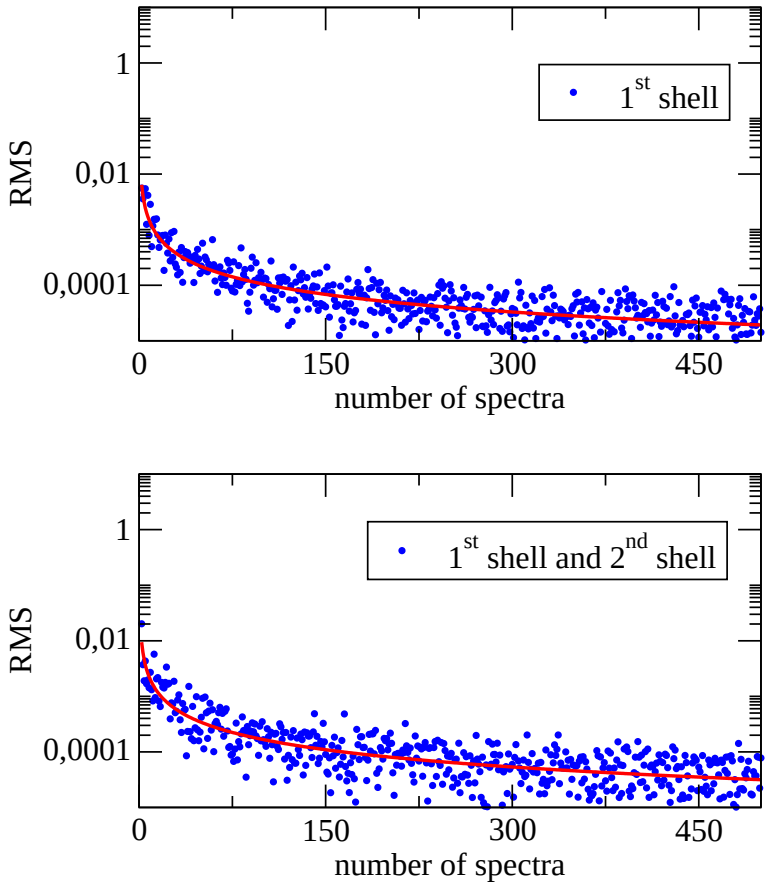

Figure 4.1: Residual function RMS of the L_3-edge XANES averaged spectra for Yb(III) as a function of MD snapshots including the first only (upper panel) and first plus second hydration shells (lower panel).

4.1.3 EXAFS data analysis

In the standard EXAFS analysis of disordered systems only two-body distributions are usually included, and the $\chi(k)$ signal is represented by the equation 2.5. As already mentioned in section 2.2, $\chi(k)$ theoretical signals can be calculated by introducing in equation 2.5 the model radial distribution functions obtained from Molecular Dynamics simulations. In all the aqueous solutions studied, both the M-O and M-H g(r)'s obtained from the simulations have been used to calculate the single scattering first shell $\chi(k)$ theoretical signal, as the ion-hydrogen interactions have been found to provide a detectable contribution to the EXAFS spectra of several metal ions in aqueous solutions [80, 81]. Comparison of the total theoretical and experimental $\chi(k)$ signals allows the reliability of the g(r)'s, and consequently of the theoretical scheme used in the simulations, to be checked. In this case, i.e. when a direct comparison between the signal obtained from Molecular Dynamics simulations and the experimental one is performed, the structural parameters are kept fixed during the minimization, while two nonstructural parameters are optimized: S_0^2, which is a many-body amplitude reduction factor due to intrinsic losses, and E_0, which aligns the experimental and theoretical energy scales. On the other hand, the theoretical $\chi(k)$ signal can also be refined against the experimental data in order to obtain the better possible agreement between the two spectra. In this latter case, the fitting is performed by using a least-squares minimization procedure in which structural and nonstructural parameters are allowed to float [82]. Since a correct description of the first coordination sphere of hydrated metal complexes has to account for the asymmetry in the distribution of the ion-solvent distances, the M-O and M-H g(r)'s associated with the first coordination shells were modeled with Γ-like distribution functions which depend on four parameters, namely the coordination number N_c, the average distance R, a standard deviation σ, and the skewness (see section 2.2).

The EXAFS theoretical signals have been calculated by means of the GNXAS code which uses an advanced theoretical scheme based on the multiple-scattering formalism [48]. Phase shifts, A(k,r) and ϕ(k,r), have been calculated starting from a configuration extracted from the Molecular Dynamics simulation, by using muffin-tin potentials and advanced models for the exchange-correlation self-energy (Hedin-Lundqvist) [47]. Inelastic losses of the photoelectron in the final state have been accounted for intrinsically by complex potential. The imaginary part also includes a constant factor accounting for the core-hole width.

4.2 MD simulations

MD simulations of Nd(III), Gd(III), and Yb(III) ions in aqueous solution have been performed using the ab initio effective two-body potentials developed by Floris et al. [5], obtained by fitting the parameters of a suitable analytical function on an ab initio potential energy surface. The SPC/E

water intramolecular potential was used in the fitting procedure [83]. Three uncharged massless interaction sites were added to the water molecule: two of these (L_1 and L_2) are symmetrically located on the axis going through the O atom, perpendicular to the water molecular plane; the third virtual site (L_3) is on the C_2 axis on the opposite side with respect to the hydrogen atoms. A thorough description of the procedure used to obtain the ab initio potential energy function can be found in ref [5]. The potential functions have the following analytical form:

$$U_{Mi}(r) = U_{Coul} + A_i r_{Mi}^{-4} + B_i r_{Mi}^{-6} + C_i r_{Mi}^{-8} + D_i r_{Mi}^{-12} + F_i e^{-G_i r_{Mi}} \quad (4.1)$$

where U_{Coul} is the Coulomb interaction computed with atomic charges as in the SPC/E model [83], M stands for one of three lanthanoid ions and i is an interaction site on water, that is, the water oxygen and hydrogen atoms and the three dummy atoms and r_{Mi} is the ion-interaction site distance. A_i,..., G_i are the potential function parameters obtained by the fitting procedure (see Table 2 of ref [5]). The simulated systems were composed by one Ln(III) ion and 809 water molecules (for a total of 4855 atoms and virtual interaction sites) in a cubic box, using periodic boundary conditions. The box side was always 29.054 Å. All simulations were performed in a NVT ensemble at 300 K using the Berendsen method [84] with a coupling constant of 0.01 ps. A time step of 1 fs was used, saving a configuration every 25 time steps. Calculations were carried out using the GROMACS package version 3.2.1 [85] modified to include the effective pair potentials. Short-range interactions have been truncated at 9 Å and the Particle Mesh Ewald [66, 67] method was employed to treat long-range electrostatic effects while an homogeneous background charge has been used to compensate for the presence of the Ln(III) ion [86]. MD simulations of 5 ns were used to sample each of the three systems, after an equilibration phase of 1 ns.

4.3 Polarised MD simulations

MD simulations of lanthanoids ions in aqueous solution, taking into account the polarization, have been performed using the procedure developed by M. Duvail et al. described in references [58]. The total potential energy of the system is modeled as a sum of different terms:

$$V_{tot} = V_{elec} + V_{O-O}^{LJ} + V_{Ln-O} \quad (4.2)$$

where V_{elec} is the electrostatic energy term defined by equation 3.10 and V_{O-O} is the 12-6 Lennard-Jones potential describing the O-O interaction. Because of the explicit polarization introduced in the model, the original TIP3P water [87] was modified into the TIP3P/P water model [16], i.e., the charges on O and H were rescaled to reproduce correctly the dipole moment of liquid water. V_{Ln-O} account for the *nonelectrostatic* Ln-O interaction potential. The potential is composed by a long range attractive part with a $1/r^6$ behavior and a

short range repulsive part modeled via an exponential function, dealing with the well-known Buckingham exponential-6 potential (Buck6):

$$V_{ij}^{Buck6} = A_{ij}exp(-B_{ij}r_{ij}) - \frac{C_{ij}}{r_{ij}^6} \tag{4.3}$$

The Ln-O Buck6 parameters are estimated from extrapolating the original La-O Buck6 parameters obtained by fitting the Møller-Plesset perturbation (MP2) potential energy curve [16], while for all the other lanthanoid ions the Buck6 parameters were extrapolated using the Shannon ionic radii [88].
Simulations of the hydrated Ln(III) ions have been carried out in the micro-canonical NVE ensemble with a own developed classical molecular dynamics CLMD code MDVRY [89] using a Car-Parrinello-like scheme to obtain atomic induced dipoles [90].
CCLMD simulations were performed for one Ln(III) and 216 rigid water molecules in a cubic box at room temperature. As previously reported [16] test simulations with a 1000 water molecules box provide the same results and thus was used this relatively small box to simulate many systems with also different sets of parameters for each system. Simulations were done on a 2.4 GHz AMD Opteron CPU and each simulation takes about 10 h/ns. Periodic boundary conditions were applied to the simulation box. Long-range interactions have been calculated by using smooth particle mesh Ewald method [67]. Simulations were performed using a velocity-Verlet-based multiple time scale for the simulations with the TIP3P/P water model. Equations of motion were numerically integrated using a 1 fs time step. The system was equilibrated at 298 K for 2 ps. Production runs were subsequently collected for 3 ns. The average temperature was 293 K with a standard deviation of 10 K.

Chapter 5

Structures of solvated Nd(III), Gd(III), Yb(III) and Lu(III) in aqueous solution and crystalline salts

5.1 Hydrated lutetium(III) ions in aqueous solution and in the trifluoromethanesulfonate salt

To shed light on the geometry of the hydration complex of the Ln(III) ions in aqueous solution, a useful strategy is to use solid salts of known structure as starting coordination models. To this end we have collected the XANES spectra at the K- and L_3-edge of $[Lu(H_2O)_{8.2}](CF_3SO_3)_3$. This compound has been chosen because the water molecules in the first coordination shell are arranged in a distorted TTP geometry. In the low-temperature structure, the six Lu-O bond lengths in the fairly regular trigonal prism are in the range 2.272(4)-2.296(4) Å, one capping site is fully occupied with a Lu-O length of 2.395(4) Å, whereas for the two more distant capping sites the Lu-O distances are 2.555(6) and 2.568(6) Å with occupancy factors of 0.58(1) and 0.59(1), respectively [15]. The high-temperature phase can be regarded as an average of the low-temperature structure as previously discussed [15]. This is further supported by the fact that the structure of the high-temperature phase as determined by EXAFS, which is lattice independent, is in full agreement with the low-temperature phase. This shows that the geometry of the hydrated lutetium(III) ion observed in the low-temperature phase is also present at room temperature and in aqueous solution [15]. The raw K-edge spectrum of solid $[Lu(H_2O)_{8.2}](CF_3SO_3)_3$ is compared with the spectrum of lutetium(III) in aqueous solution in the upper panel of Figure 5.1. The two spectra are identical in the whole energy range suggesting that the coordination of the lutetium(III) ion in the two systems is the same. However, owing to the short lifetime of the excited atomic state, both the edge resonance and the struc-

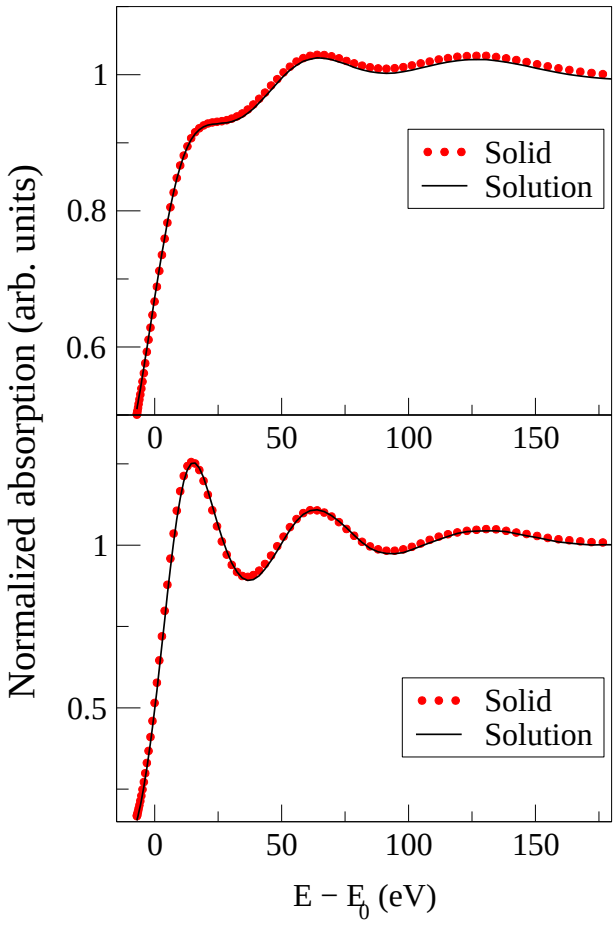

Figure 5.1: Upper panel: Comparison between the raw K-edge XANES spectra of lutetium(III) in aqueous solution (solid line) and solid $[Lu(H_2O)_{8.2}](CF_3SO_3)_3$ (red dotted line). Lower panel: Comparison between the K-edge deconvolved XANES spectra of lutetium(III) in aqueous solution (solid line) and solid $[Lu(H_2O)_{8.2}](CF_3SO_3)_3$ (dotted red line).

tural oscillations are strongly damped. Therefore, we have applied a core-hole width deconvolution procedure [77] to the XANES spectra of both the solid and aqueous solution samples. The whole tabulated core-hole width (Γ=33.7 eV) [76] has been removed from the K-edge raw experimental data, and a Gaussian filter with full width at half maximum of about 14 eV has been applied. After deconvolution, the threshold regions are considerably sharpened with respect to the original spectra, and the intensity of the structural oscillations is also clearly enhanced (see lower panel of Figure 5.1). Also, in this case the XANES spectrum of lutetium(III) in aqueous solution is identical to the solid lutetium(III) trifluoromethanesulfonate one, reinforcing the similarity of the first-neighbor coordination geometry. In the first step of the analysis, the reliability of the MXAN method has been tested by applying a minimization procedure to both the raw and deconvolved K-edge XANES spectra of

solid lutetium(III) trifluoromethanesulfonate. The analysis has been carried out starting from the low-temperature crystallographic structure [15], and by refining the structural and nonstructural parameters. In the fits, eight water molecules were included: six in the prism sites at the same distance and two in the capping sites with different Lu-O bond lengths. Note that the hydrogen atoms have been included in the analysis. The results of the fitting procedures are shown in Figure 5.2 for the raw and deconvolved spectra, and the bond metrics are detailed in Table 5.1.

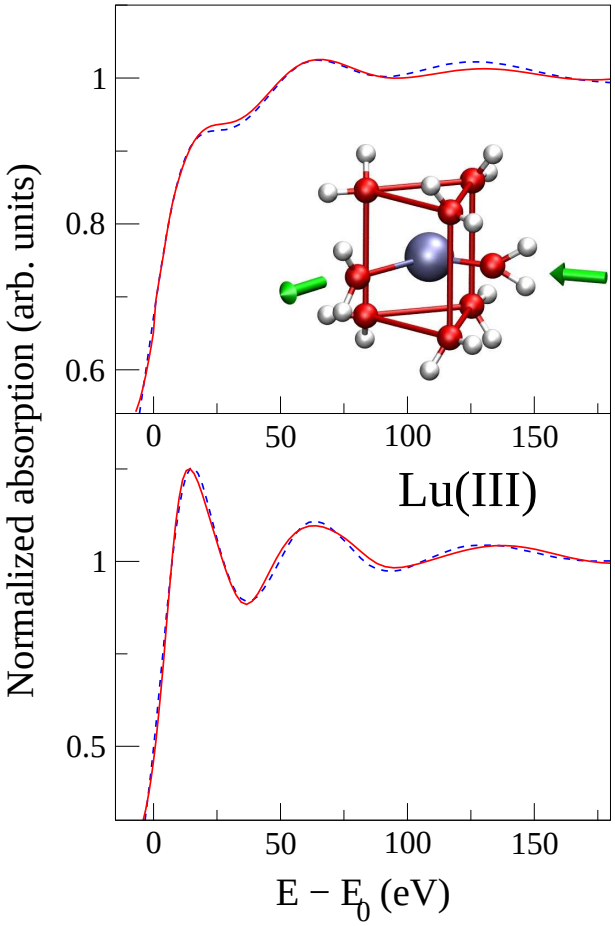

Figure 5.2: Upper panel: Comparison between the raw K-edge XANES experimental spectrum of solid $[Lu(H_2O)_{8.2}](CF_3SO_3)_3$ (dashed blue line) and the theoretical spectrum including the first coordination shell only (solid red line). Lower panel: Comparison between the K-edge XANES deconvolved experimental spectrum of solid $[Lu(H_2O)_{8.2}](CF_3SO_3)_3$ (dashed blue line) and the theoretical spectrum including the first coordination shell only (solid red line).

The agreement between the experiment and the calculated model is quite good in the case of the raw data [R_{sq}=2.3, in which R_{sq} is the square residual function, see Eq. 2.7] and it improves for the deconvolution spectrum (R_{sq}= 1.2). It is known that systematic errors in the MXAN analysis can

arise mostly because of the poor approximation used for the phenomenological broadening function Γ(E) that mimics the electronic damping [55, 91, 92]. This can explain the better agreement between the experimental and calculated spectrum obtained for the deconvolved data. Note that the structural parameters obtained from the two analyses are equal within the statistical errors, and are in good agreement with the crystallographic determination. However, as expected, the statistical errors obtained from the minimization are slighter larger in the case of the raw data, as compared with the deconvolved data. As far as the non structural parameters are concerned, the Γ values obtained from the raw and deconvolved data are 26 and 10 eV, respectively.

Fitting procedures have also been applied to the raw and deconvolved XANES spectra of the aqueous solution of lutetium(III) by using the low-temperature crystallographic structure of $[Lu(H_2O)_{8.2}](CF_3SO_3)_3$ as a starting model. The best-fit results are identical to those obtained for the trifluoromethanesulfonate crystal, both for the raw and deconvolved data (see Table 5.1).

A different picture emerges from the comparison between the L_3-edge XANES spectra of lutetium(III) in aqueous solution and solid trifluoromethanesulfonate (Figure 5.3). In this case, the two spectra show sizeable differences both in the edge and higher-energy region. In particular, both spectra have a sharp main peak followed by the structural oscillations, but the solid sample shows two additional humps at about 18 and 48 eV that are not present in the aqueous solution spectrum. To unveil the origin of this difference we have carried out a quantitative analysis of the L_3-edge XANES data along the line of the K-edge investigation. The MXAN analysis of the L_3-edge of solid lutetium(III) trifluoromethanesulfonate was begun, again by including the eight water molecules of the first coordination sphere only, starting with the crystallographic metrics. The results are shown in the upper panel of Figure 5.4, in which the experimental data are compared with the calculated best fit. In this case, even if the main features of the spectrum are well accounted for, the quality of the fit is not satisfactory (R_{sq}=3.8) and the main discrepancy between the theoretical and experimental spectra is the lack of the two bumps at about 18 and 48 eV. This failure of the model indicates a need to enlarge the number of atoms used in the calculation, and the likelihood that the second coordination shell contributes to the XANES energy region. Therefore, we carried out a second fit including all of the atoms within a distance of 5.5 Å from the lutetium(III) ion. This new fit shows substantial improvement in quality (R_{sq}=2.0) and the inclusion of the second shell structure leads to the appearance of the previous missing features (lower panel of Figure 5.4). The structural best-fit results compare well with the crystallographic determination (Table 5.1 and Table 2 of ref [15]). The very good agreement between the calculated and experimental spectra gives strong support to the reliability of the MXAN method when applied to the analysis of the L_3-edges.

To examine the compatibility of the aqueous solution L_3-edge XANES

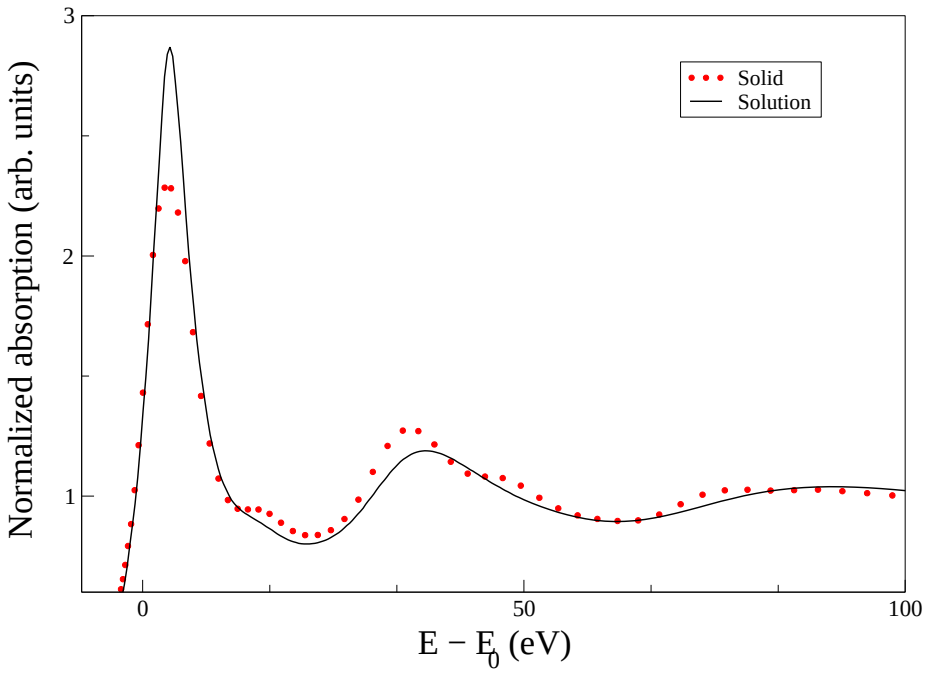

Figure 5.3: Comparison between the L_3-edge XANES spectra of lutetium(III) in aqueous solution (solid line) and solid $[Lu(H_2O)_{8.2}](CF_3SO_3)_3$ (red dotted line).

spectrum with the existence of a distorted TTP geometry of the solvated lutetium(III) ion, we performed a minimization of the experimental data that only included the first hydration shell by using the distorted eight-fold TTP geometry of the crystal. In this case, a very good reproduction of the spectrum was obtained with the crystallographic metrics (R_{sq}=1.8; upper panel of Figure 5.5 and Table 5.1) and the second hydration shell does not provide any detectable contribution to the XANES. For the sake of completion, we have also tested the possibility of having a SAP coordination for the lutetium(III) hydration complex. To this end we carried out an additional fit imposing a regular SAP geometry with eight equal Lu-O bond lengths, and the results of this analysis are shown in the lower panel of Figure 5.5. In this case, a best-fit Lu-O bond length of 2.31 Å has been obtained with a poor agreement between the experimental and theoretical spectra (R_{sq}=4.0), especially in the energy region above 20 eV.

Altogether, these findings demonstrate that the lutetium(III) ion in aqueous solution forms an hydration complex that has a distorted TTP geometry with six water molecules in the prismatic positions at about 2.27 Å, and two additional water molecules in the capping sites with different Lu-O bond lengths (2.37 and 2.56 Å, respectively).

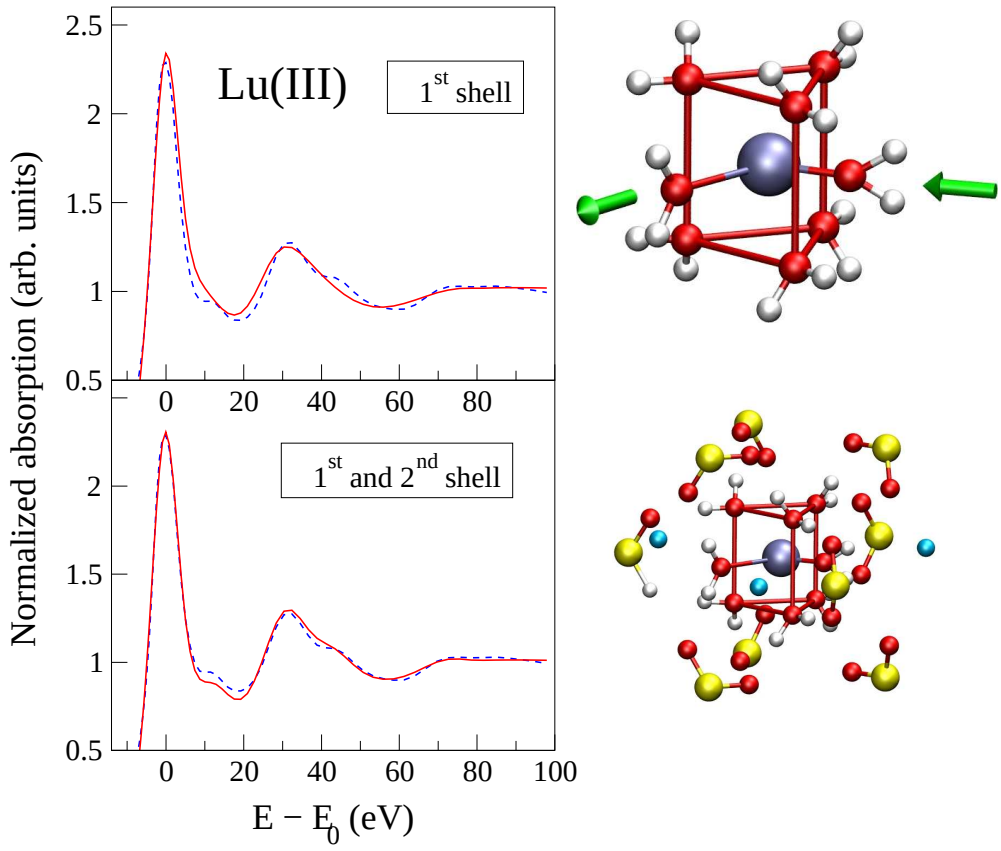

Figure 5.4: Upper panel: Comparison between the L_3-edge XANES experimental spectrum of solid $[Lu(H_2O)_{8.2}](CF_3SO_3)_3$ (dashed blue line) and the theoretical spectrum including the first coordination shell, only (solid red line). Lower panel: Comparison between the L_3-edge XANES experimental spectrum of solid $[Lu(H_2O)_{8.2}](CF_3SO_3)_3$ (dashed blue line) and the theoretical spectrum including the first plus second coordination shells (solid red line).

5.2 Hydrated Nd(III), Gd(III) and Yb(III) ions in aqueous solution and in the trifluoromethanesulfonate salt

A complete picture of the hydration properties of the Ln(III) ions along the series has been obtained by analyzing the XANES spectra at the K- and L_3-edges of three additional ions that have different coordination properties, namely, neodymium(III), gadolinium(III) and ytterbium(III). As already found for lutetium(III), the neodymium(III), gadolinium(III) and ytterbium(III) raw and deconvolved K-edge XANES spectra in aqueous solution and in solid trifluoromethanesulfonate salts are identical (see Figure 5.6). Also in this case a quantitative analysis of the K-edge XANES spectra has been carried out starting from the crystallographic structure of the solid tri-

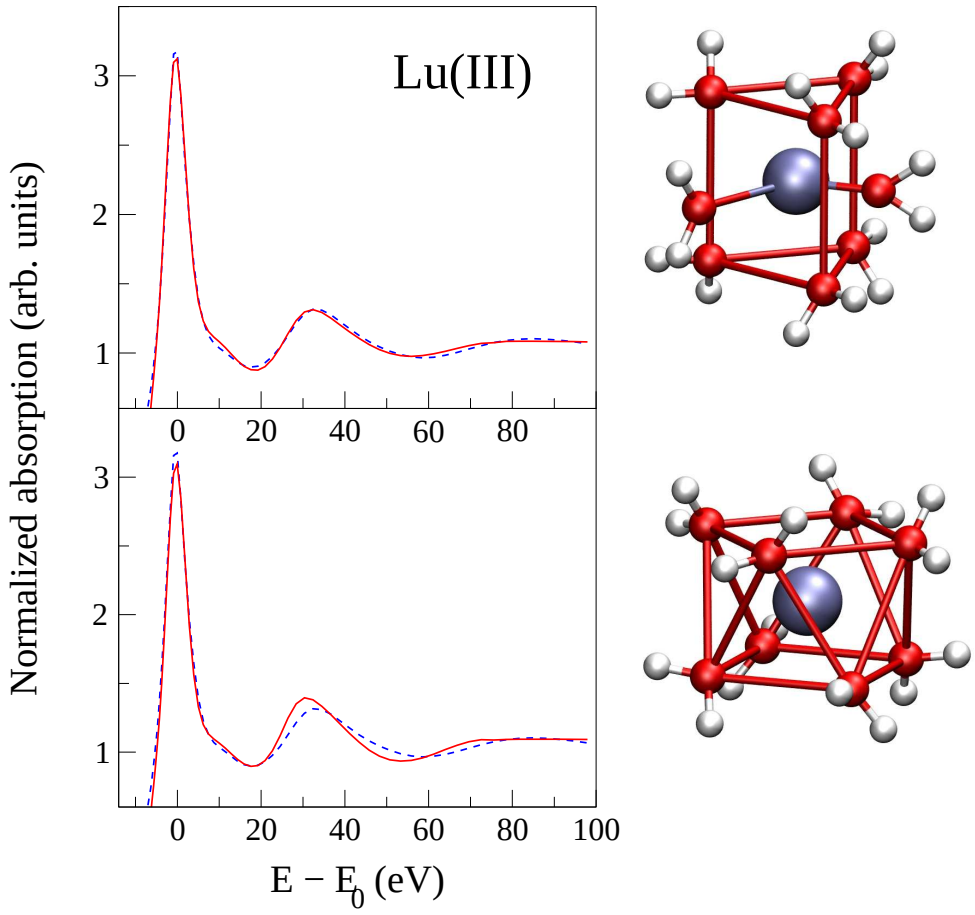

Figure 5.5: Upper panel: Comparison between the L_3-edge XANES experimental spectrum of lutetium(III) in aqueous solution (dashed blue line) and the theoretical spectrum associated with a bicapped trigonal prismatic configuration of the first hydration shell (solid red line). Lower panel: Comparison between the L_3-edge XANES experimental spectrum of lutetium(III) in aqueous solution (dashed blue line) and the theoretical spectrum associated with a square antiprismatic configuration of the first hydration shell (solid red line).

fluoromethanesulfonate salts by only including the first coordination shell. In particular, in the $[Nd(H_2O)_9](CF_3SO_3)_3$ crystal the neodymium(III) ion is surrounded by nine water molecules arranged in a regular TTP configuration with six prismatic and three capping Nd-O bonds with bond lengths of 2.451 and 2.569 Å, respectively [93]. In the $[Gd(H_2O)_9](CF_3SO_3)_3$ crystal, the prismatic Gd-O bond lengths are equal to 2.397 Å whereas the water molecules in the capping sites coordinate the ion at a distance of 2.538 Å[93].In the $[Yb(H_2O)_9](CF_3SO_3)_3$ crystal, the prismatic Yb-O bond lengths are equal to 2.302 Å whereas the water molecules in the capping sites coordinate the ion at a distance of 2.532 Å[93]. No phase transition to lower space-group

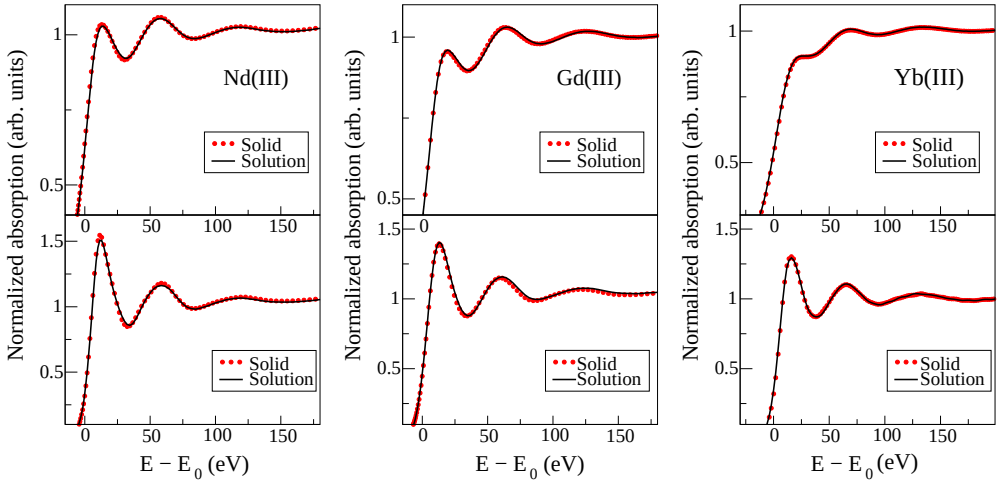

Figure 5.6: The upper panels of each figures show the comparison between the raw K-edge XANES spectra of neodimium(III), gadolinium(III) and ytterbium(III) in aqueous solution (solid line) and in solid trifluoromethanesulfonate salts (red dotted line). The lower panels show the comparison between the raw K-edge deconvolved XANES spectra of neodimium(III), gadolinium(III) and ytterbium(III) in aqueous solution (solid line) and in solid trifluoromethanesulfonate salts (red dotted line).

symmetry was observed at low-temperature for the hydrated lanthanoid(III) trifluoromethanesulfonate salts with full occupancy in the capping positions. In Figure 5.7, the results of the minimization procedure applied to the K-edge XANES raw and deconvolved data spectra of neodymium(III) aqueous solution are reported. In these cases the agreement between the experimental and theoretical data is very good, and the structural results compare very well with the crystallographic metrics (see Table 5.1).

A different strategy has been used for the analysis of the XANES data of gadolinium(III) and ytterbium(III) based on the results of a previous combined crystallographic and EXAFS investigation [15]. This study has shown that for the medium-sized lanthanoid(III) ions (Sm-Ho) the mean capping bond lengths from the EXAFS data are somewhat shorter than the crystallographic results with a full occupancy in the capping positions, while for the heavy lanthanoid(III) ions (Er-Lu) water deficiency in the three capping positions starts at holmium(III) and increases for erbium(III), thulium(III), ytterbium(III) and lutetium(III). This deviation has been explained with the existence of a slightly distorted molecular configuration, probably with one capping water molecule that is more strongly bound to the ion. For this reason, the XANES spectra of the gadolinium(III) and ytterbium(III) ion have been analyzed by imposing the same prismatic Gd-O and Yb-O bond lengths while refining the three capping water molecules independently. For Gd the best-fit structure obtained from the minimization resulted in a distorted TTP complex with one water molecule in the capping site coordinating the ion at a slightly shorter distance (2.49 Å) as compared with the other two capping molecules (2.54 Å), and for Yb a TTP complex with three different distances of the capping sites (2.54, 2.44 and 2.39 Å). Figures 5.8, 5.9 a) and 5.9 c)

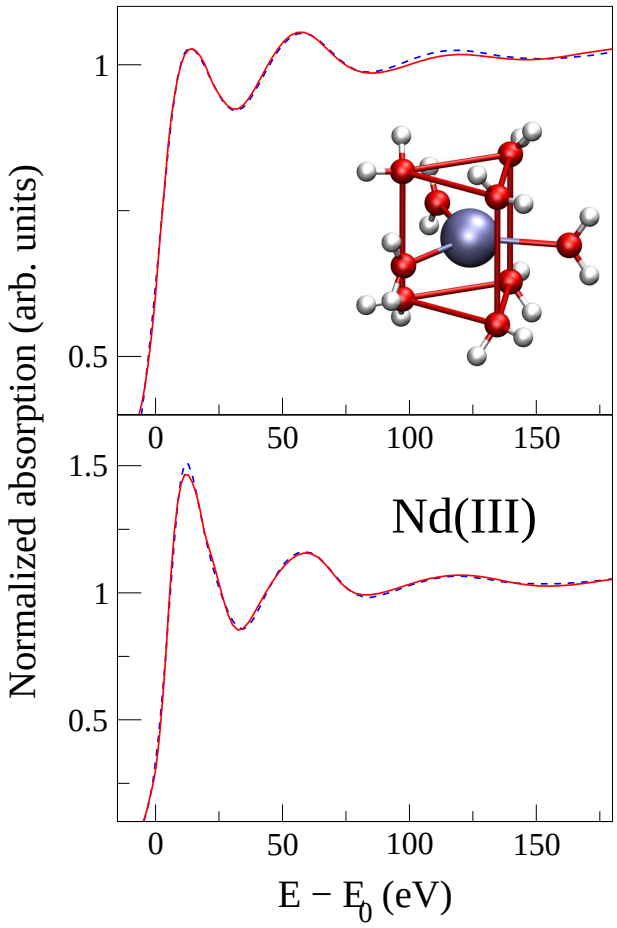

Figure 5.7: Upper panel: Comparison between the K-edge raw XANES experimental spectrum of neodymium(III) in aqueous solution (dashed blue line) and the theoretical spectrum including the first coordination shell, only (solid red line). Lower panel: Comparison between the K-edge deconvolved XANES experimental spectrum of neodymium(III) in aqueous solution (dashed blue line) and the theoretical spectrum including the first coordination shell, only (solid red line)..

depict the comparison between the experimental (raw and deconvolved data) K-edge spectra of gadolinium(III) and the deconvolved K-edge only spectrum of ytterbium(III) in aqueous solution and the theoretical calculations. The agreement is very good and the best-fit structure results are listed in Table 5.1.

Very similar results were obtained for the three ions from the analysis of the solid trifluoromethanesulfonate salts (Table 5.1). The comparison of the L_3-edges of the solid samples and aqueous solution shows remarkable differences (see Figure 5.10).

In particular, the intensity of the white line and the overall shape of these spectra are different, and the quantitative analysis of the spectra allowed us, once more, to shed light on the origin of this phenomenon. Two different

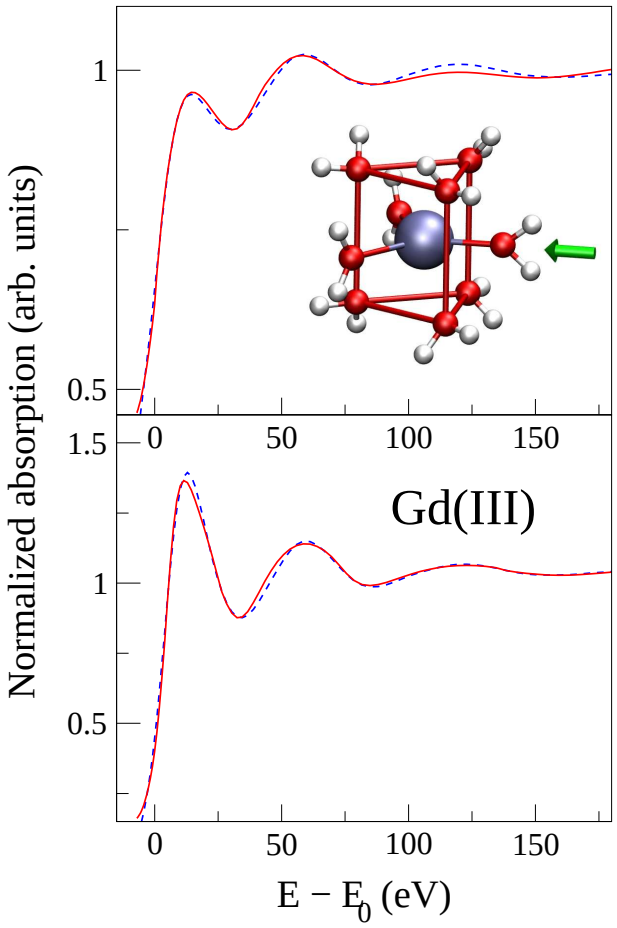

Figure 5.8: Upper panel: Comparison between the K-edge raw XANES experimental spectrum of gadolinium(III) in aqueous solution (dashed blue line) and the theoretical spectrum including the first coordination shell, only (solid red line). Lower panel: Comparison between the K-edge deconvolved XANES experimental spectrum of gadolinium(III) in aqueous solution (dashed blue line) and the theoretical spectrum including the first coordination shell, only (solid red line).

analyses have been carried out on the solid trifluoromethanesulfonate spectra at the L_3- edge, the former only including the first coordination shell and the latter including all of the atoms surrounding the ions up to a distance of 5.5 Å. Also, in this case the agreement between the theoretical and experimental spectra improves when the second coordination shell is included in the calculations (see Figures 5.11, 5.9 b), 5.9 c) and Table 5.1).

In the last step of the analysis, least-squares fits of the L_3- edge XANES spectra of neodymium(III) gadolinium(III) and ytterbium(III) in aqueous solution were carried out by assuming the existence of a regular (for the neodymium(III)) and distorted TTP (for gadolinium(III) and ytterbium(III)) hydration complex ion. The best-fit XANES spectra are compared with the experimental data in Figure 5.12. Note that at variance with the lutetium(III)

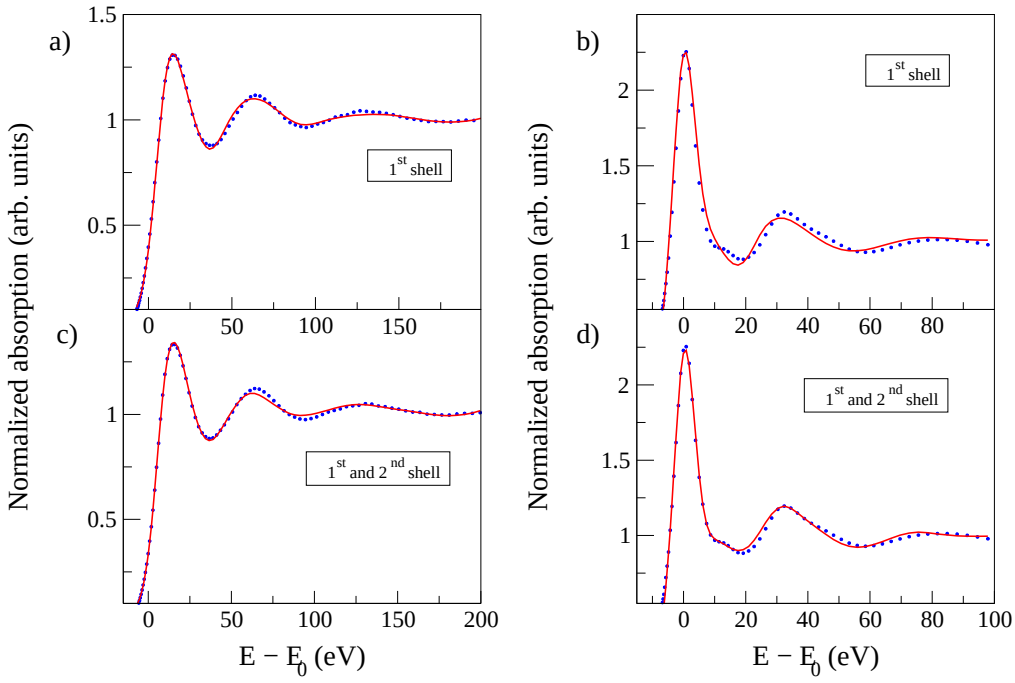

Figure 5.9: a) Comparison between the deconvolved K-edge XANES experimental spectrum of solid $[Yb(H_2O)_{8.7}](CF_3SO_3)_3$ (dotted blue line) and the best-fit theoretical spectrum including only the first hydration sphere (solid red line); b) Comparison between the L_3-edge XANES experimental spectrum of solid $[Yb(H_2O)_{8.7}](CF_3SO_3)_3$ (dotted blue line) and the best-fit theoretical spectrum including only the first hydration sphere (solid red line); c) Comparison between the deconvolved K-edge XANES experimental spectrum of solid $[Yb(H_2O)_{8.7}](CF_3SO_3)_3$ (dotted blue line) and the best-fit theoretical spectrum including both the first and second hydration shells (solid red line); d) Comparison between the L_3-edge XANES experimental spectrum of solid $[Yb(H_2O)_{8.7}](CF_3SO_3)_3$ (dotted blue line) and the best-fit theoretical spectrum including both the first and second hydration shells (solid red line).

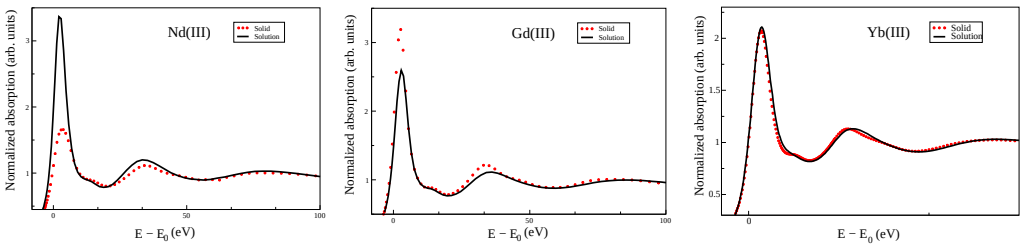

Figure 5.10: Comparison between the L_3-edge XANES spectra of neodimium(III) (left panel), gadolinium(III)(middle panel) and ytterbium(III)(right panel) in aqueous solution (solid line) and in solid trifluoromethanesulfonate salts (red dotted line).

results, in this case it was not possible to perfectly reproduce the experimental spectra by only using the first hydration shell cluster. This finding points out the need to include the second hydration shell in the XANES theoretical calculation to get a good agreement with the experimental data of the aqueous solution samples.

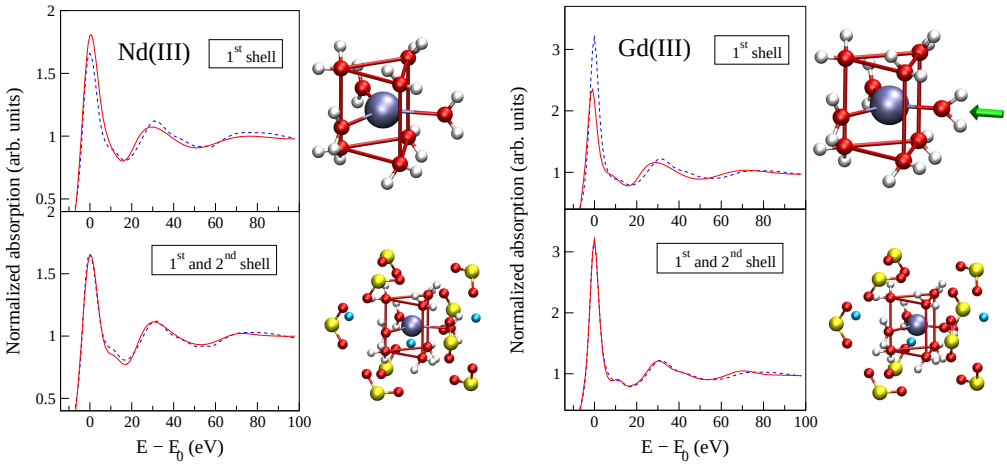

Figure 5.11: Top left panel:Comparison between the L_3 XANES experimental spectrum of solid $[Nd(H_2O)_9](CF_3SO_3)_3$ (dashed blue line) and the theoretical spectrum including the first coordination shell, only (solid red line). Lower left panel: Comparison between the L_3 XANES experimental spectrum of solid $[Nd(H_2O)_9](CF_3SO_3)_3$ (dashed blue line) and the theoretical spectrum including the first plus second coordination shells (solid red line). Top right panel: Comparison between the L_3 XANES experimental spectrum of solid $[Gd(H_2O)_9](CF_3SO_3)_3$ (dashed blue line) and the theoretical spectrum including the first coordination shell, only (solid red line). Lower right panel: Comparison between the L_3 XANES experimental spectrum of solid $[Gd(H_2O)_9](CF_3SO_3)_3$ (dashed blue line) and the theoretical spectrum including the first plus second coordination shells (solid red line).

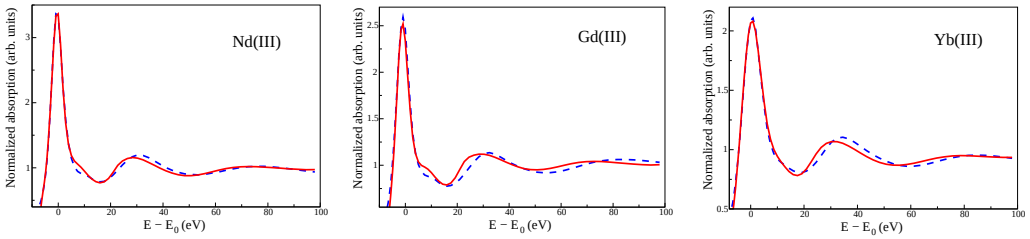

Figure 5.12: Comparison between the L_3 XANES experimental spectrum of neodymium(III)(left panel), gadolinium(III)(middle panel) and ytterbium(III)(right panel) in aqueous solution (dashed blue line) and the theoretical spectrum associated with a tri-capped trigonal prismatic configuration of the first hydration shell (solid red line).

Table 5.1: K- and L_3-edge XANES structural parameters of the hydrated lutetium(III), neodymium(III), gadolinium(III) and ytterbium(III) ions in the solid trifluoromethanesulfonate salts and in slightly acidic aqueous solutions. Ln-O_p is the distance between the ion and the six equivalent oxygen atoms in the prismatic sites, Ln-O_{c1}, Ln-O_{c2}, and Ln-O_{c3} are the distances between the ion and each capping oxygen atom. Distances are in Å while Γ_c are in eV. The EXAFS determinations are reported for comparison.[15]

	K-edge data					L_3-edge data				
	Ln-O_p	Ln-O_{c1}	Ln-O_{c2}	Ln-O_{c3}	Γ_c	Ln-O_p	Ln-O_{c1}	Ln-O_{c2}	Ln-O_3	Γ_c
Lu(III) trifluoromethanesulfonate (solid)										
XANES	2.31(6)	2.34(5)	2.60(5)		25.8	2.28(2)	2.34(3)	2.59(3)		5.0
XANES dec	2.27(3)	2.33(4)	2.61(3)		9.8					
EXAFS	2.30(1)	2.37(2)*				2.32(4)	2.37(4)*			
Lu(III)/water										
XANES	2.31(5)	2.34(5)	2.60(5)		30.3	2.25(3)	2.37(2)	2.56(3)		4.7
XANES dec	2.26(2)	2.33(4)	2.61(4)		10.0					
EXAFS	2.29(1)	2.35(2)*				2.28(4)	2.37(4)*			
Nd(III) trifluoromethanesulfonate (solid)										
XANES	2.48(5)	2.57(5)	2.57(5)	2.57(5)	15.3	2.44(2)	2.56(2)	2.56(2)	2.56(2)	3.7
XANES dec	2.44(2)	2.56(4)	2.56(4)	2.56(4)	2.5					
EXAFS	2.47(1)	2.57(2)*				2.48(4)	2.58(4)*			
Nd(III)/water										
XANES	2.45(5)	2.57(5)	2.57(5)	2.57(5)	15.3	2.46(2)	2.57(2)	2.57(2)	2.57(2)	3.7
XANES dec	2.44(2)	2.56(3)	2.56(4)	2.56(4)	2.9					
EXAFS	2.48(1)	2.57(2)*				2.47(4)	2.60(4)*			

* Mean capping bond length

	K-edge data					L_3-edge data			
	Ln-O_p	Ln-O_{c1}	Ln-O_{c2}	Ln-O_{c3}	Γ_c	Ln-O_p	Ln-O_{c1}	Ln-O_{c2}	Ln-O_3	Γ_c
Gd(III) trifluoromethanesulfonate (solid)										
XANES	2.39(4)	2.54(5)	2.54(5)	2.49(5)	20.4	2.39(2)	2.54(2)	2.54(2)	2.49(2)	4.7
XANES dec	2.37(4)	2.54(4)	2.54(4)	2.49(4)	6.2					
EXAFS	2.41(1)	2.53(2)*				2.41(4)	2.35(4)*			
Gd(III)/water										
XANES	2.37(6)	2.54(5)	2.54(5)	2.49(5)	19.9	2.40(4)	2.54(4)	2.54(4)	2.49(5)	3.7
XANES dec	2.37(3)	2.53(4)	2.53(4)	2.47(4)	6.4					
EXAFS	2.41(1)	2.55(2)*				2.40(4)	2.53(4)*			
Yb(III) trifluoromethanesulfonate (solid)										
XANES						2.30(2)	2.54(2)	2.44(2)	2.39(2)	5.0
XANES dec	2.26(4)	2.54(4)	2.44(4)	2.39(4)	4.6					
EXAFS	2.32(1)	2.46(2)*				2.32(4)	2.43(4)*			
Yb(III)/water										
XANES						2.30(4)	2.54(4)	2.44(4)	2.39(5)	4.0
XANES dec										
EXAFS						2.31(4)	2.43(4)*			

* Mean capping bond length

Table 5.2: Non-structural parameters as determined by MXAN. E_F (eV) is the Fermi energy level, E_s (eV) is the plasmon energy, A_s is the plasmon amplitude, E_0 (eV) is the threshold energy, and Γ_{exp} (eV) is the experimental resolution.

	K-edge data							L_3-edge data				
	E_F	Es_1	As_1	Es_2	As_2	E_0	Γ_{exp}	E_F	Es_1	As_1	E_0	Γ_{exp}
Lu(III) trifluoromethanesulfonate (solid including the first coordination shell only)												
	3.5	6.0	10.2	15.2	13.8	5.4	1.0	-1.0	80.0	80.0	5.7	2.2
DEC	-2.7	25.1	3.2			1.2	2.3					
Lu(III) trifluoromethanesulfonate (solid including both the first and the second coordination shell)												
								-1.0	79.7	80.0	5.7	2.2
Lu(III)/water												
	5.1	8.1	12.4	10.3	9.8	5.0	1.0	-1.8	75.0	80.0	5.1	1.2
DEC	-1.8	26.8	1.0			-1.4	2.3					
Nd(III) trifluoromethanesulfonate (solid including the first coordination shell only)												
	-4.8	1.4	27.5	22.5	5.3	-5.0	1.1	-1.0	21.9	12.2	5.7	2.1
DEC	-3.3	14.8	6.3			-2.1	2.0					
Nd(III) trifluoromethanesulfonate (solid including both the first and the second coordination shell)												
								-1.0	21.9	12.2	5.7	2.1
Nd(III)/water												
	-3.1	2.3	44.3	19.6	4.5	0.2	1.1	-7.7	15.3	6.2	6.4	0.8
DEC	-3.3	14.8	6.3			-2.1	1.8					

	K-edge data							L_3-edge data				
	E_F	Es_1	As_1	Es_2	As_2	E_0	Γ_{exp}	E_F	Es_1	As_1	E_0	Γ_{exp}
Gd(III) trifluoromethanesulfonate (solid including the first coordination shell only)												
	2.6	2.8	33.7	40.5	5.5	-1.1	1.0	-7.3	15.1	4.6	3.8	0.8
DEC	-2.8	25.3	8.6			-4.3	1.6					
Gd(III) trifluoromethanesulfonate (solid including both the first and the second coordination shell)												
								-0.8	15.1	4.6	3.8	0.8
Gd(III)/water												
	-2.8	20.4	33.7	2.8	40.6	0.4	1.0	-9.9	28.8	17.9	4.6	1.3
DEC	-5.7	21.5	7.5			-1.8	2.0					
Yb(III) trifluoromethanesulfonate (solid including the first coordination shell only)												
								-1.2	7.9	6.6	4.0	2.3
DEC	0.0	15.2	2.4			-2.8	4.5					
Yb(III) trifluoromethanesulfonate (solid including both the first and the second coordination shell)												
								-1.2	7.9	6.6	4.0	2.3
DEC	2.2	10.0	6.0			-2.8	4.3					
Yb(III)/water												
								-9.9	15.2	10.1	4.2	2.7

Chapter 6

Structural and dynamic properties of neodymium(III), gadolinium(III) and ytterbium(III) ions in aqueous solution

6.1 Molecular Dynamic simulations

The structural properties of the three aqueous solution are described in terms of the metal-oxygen and metal-hydrogen radial distribution functions or g(r)'s [59]:

$$g_{AB}(r) = \frac{\langle \rho_B(r) \rangle}{\langle \rho_B \rangle_{local}} = \frac{1}{N_A \langle \rho_B \rangle_{local}} \sum_{i \in A}^{N_A} \sum_{j \in B}^{N_B} \frac{\delta(r_{ij} - r)}{4\pi r^2} \tag{6.1}$$

where $\langle \rho_B(r) \rangle$ is the particle density of type B at a distance r around particles A, $\langle \rho_B \rangle_{local}$ is the particle density of type B averaged over all the spheres around particles A with radius r_{max} (which is equal to half of the box side), N_A and N_B is the number of A and B particles, and r_{ij} is the distance between i (of type A) and j (of type B) particles. Therefore, an average over time and over the A particles is performed in the $g_{AB}(r)$ calculation. The Ln-O and Ln-H g(r)'s obtained from the MD simulations are shown in Figure 6.1 while the main structural results are collected in Table 6.1. The first peak positions of the g(r)'s show the expected lanthanoid contraction with an elongation of the first hydration shell going from Yb(III) to Nd(III). Inspection of Table 6.1 reveals that the first maximum positions of the present simulations are shorter than those obtained from Floris et al. (see Table 3 of ref [5]) and are in better agreement with the experimental results. The shortening of the Ln-O first shell distance could be due to the larger box size used in our simulations which allows a better treatment of the ion-solvent interactions. However, a direct proof of the reliability of the MD simulations has been obtained by

comparison with EXAFS experimental data.

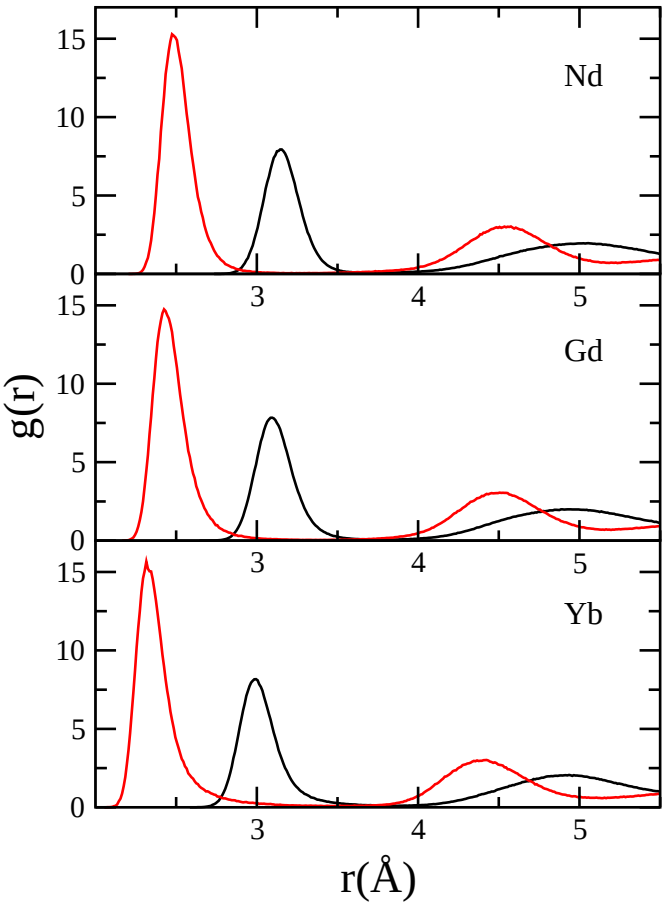

Figure 6.1: Ln-O (red line) and Ln-H (black line) radial distribution functions obtained for aqueous solutions of Nd(III), Gd(III), and Yb(III) from MD simulations.

Table 6.1: Positions (in Å) at maxima of Ln-O and Ln-H g(r)'s.

	Nd-O	Nd-H	Gd-O	Gd-H	Yb-O	Yb-H
First Maxima						
Floris et al.[5]	2.53	3.18	2.46	3.10	2.37	3.02
This work	2.48	3.15	2.43	3.09	2.32	2.99
Second Maxima						
Floris et al.[5]	4.58	5.01	4.50	4.94	4.41	4.93
This work	4.54	5.01	4.50	4.93	4.38	4.91

6.2 EXAFS Analysis

A direct comparison between MD and EXAFS results can be performed by calculating the $\chi(k)$ theoretical signal associated with the MD Ln-O and Ln-H g(r)'s by means of equation 2.5 and by comparing it with the experimental spectrum, without carrying out any minimization procedure. Here, we have used the K-edge spectra of Ln(III) ions in aqueous solutions as it has been shown that the K-edge EXAFS data provide more accurate structural results as compared to the L_3-edge ones [41]. In the upper panels of Figure 6.2 the comparison between the EXAFS experimental signal and the theoretical curves calculated using the MD g(r)'s is reported for the Nd(III), Gd(III), and Yb(III) ions. The first two curves from the top of each panel are the two-body Ln-O and Ln-H first shell contributions ($\gamma^{(2)}$) while the remainder of the figure shows the total theoretical contributions compared with the experimental spectra and the resulting residuals. The $\gamma^{(2)}$ signals are shown multiplied by k^2 for better visualization. As expected, the dominant contribution to the total EXAFS spectrum is given by the Ln-O first shell signal and, as a consequence, the EXAFS structural information is particularly accurate for the shape of the Ln-O g(r)'s first peaks, only. The Fourier transform (FT) moduli of the EXAFS $\chi(k)k^2$ theoretical, experimental, and residual signals are shown in the lower panels of Figure 6.2. The FT's have been calculated in the k-range 3.5-15.0 $Å^{-1}$ with no phase shift correction applied. The FT spectra show a prominent first shell peak which is mainly due to the Ln-O first shell distance. Nevertheless, the Ln-H FT peaks are located at about 2.4 Å, giving rise to a shoulder on the first peak. Overall, the calculated EXAFS spectra match the experimental data reasonably well in all cases showing that the structural and dynamical information derived from the MD simulations is basically correct and that the SPC/E water model provides reliable values for the ion-water distances. However, in the case of the Yb(III) ion, the agreement is slightly worse, and the residual curve shows the presence of a spurious leading frequency. This small mismatch between the experimental and theoretical curves reflects the lower accuracy of the Yb(III) MD simulation, as already pointed out by Floris et al [5].

6.3 XANES Analysis

As previously mentioned the quantitative XANES analysis of aqueous solutions can be carried out only if the structural disorder within the first hydration shell and the contribution of the higher distance coordination spheres are properly accounted for [39, 94, 40, 78, 36]. As far as the K-edge spectra are concerned, the close similarity of the solid $[Ln(H_2O)_9](CF_3SO_3)_3$ and Ln(III) aqueous solution XANES spectra (see Figure 5.6) suggests a substantial insensitivity toward the second coordination sphere. We have therefore decided to focus our attention on the L_3-edge spectra in water. The left panel of Figure 6.3 shows the averaged theoretical spectrum obtained from 500 snapshots (not including intrinsic and extrinsic inelastic process) associated with

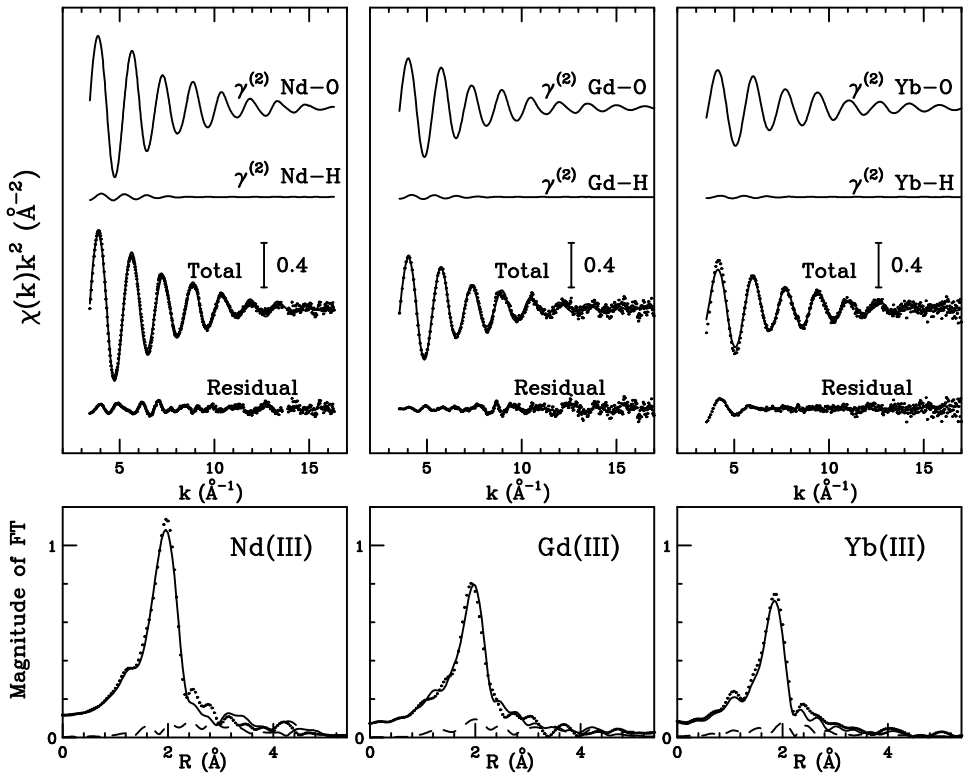

Figure 6.2: Analysis of the K-edge EXAFS spectra of aqueous solutions of Nd(III) (left panel), Gd(III) (middle panel), and Yb(III) (right panel) starting from the Ln-O and Ln-H radial distribution functions obtained from MD simulations. From the top to the bottom of each panel, the following curves are reported: the Ln-O first shell signals, the Ln-H first shell signals, the total theoretical signals compared with the experimental spectrum, and the residual curves. The lower panels show the nonphase-shift-corrected Fourier transforms of the experimental data (dotted line), of the total theoretical signals (full line), and of the residual curves (dashed-dotted line).

the first hydration shell of the hydrated Yb(III) ion, together with several individual instantaneous structures. The calculated XANES spectra present noticeable differences all along the energy range, showing the sensitivity of XANES to geometrical changes, and the importance of making a proper sampling of the configurational space. As far as the second shell is concerned our MD simulation suggests the presence of 27 water molecules up to about 6.0 Å from the Yb(III) ion. The XANES total theoretical spectrum obtained from 500 MD snapshots including both the first- and second-shell is shown in the right panel of Figure 6.3, together with several spectra computed from instantaneous configurations. In this case the individual spectra show more marked differences as compared to the first hydration shell. Considering the large deviation among instantaneous spectra it seems unlikely that a single representative configuration can be used to properly model the experimental data.

To better highlight the influence of the second hydration shell on the L_3-edge XANES spectrum of the Yb(III) ion in aqueous solution it is useful to

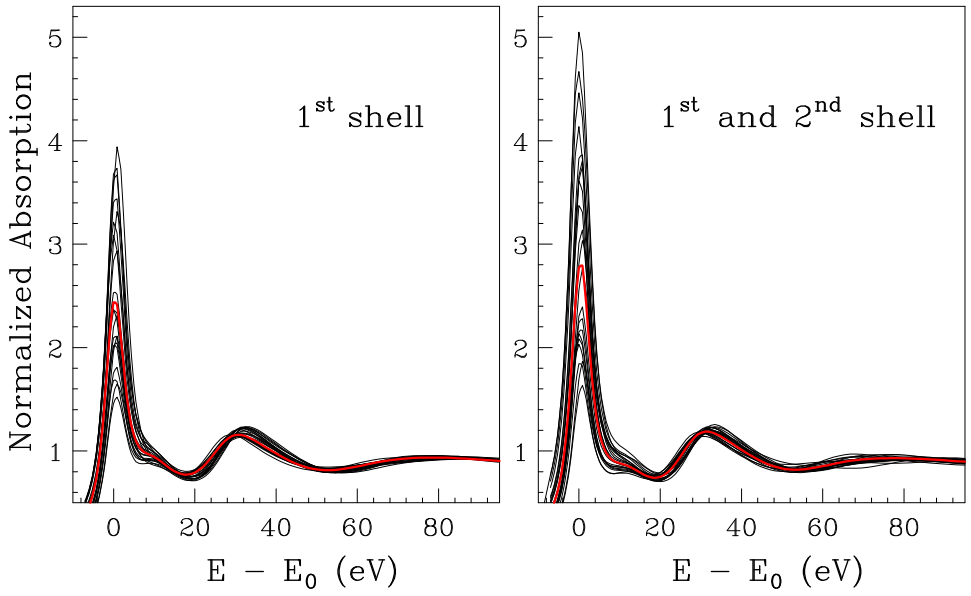

Figure 6.3: Left panel: Comparison of the theoretical XANES spectrum of the Yb(III) ion in water obtained from the MD average including only the first hydration shell (red line) and several spectra associated with individual MD configurations (black lines). Right panel: Comparison of the theoretical XANES spectrum of the Yb(III) ion in water obtained from the MD average including both the first and second hydration shells (red line) and several spectra associated with individual MD configurations (black lines).

compare the averaged spectrum calculated using first-shell-only and first- and second-shell clusters (see Figure 6.4). The calculated XANES spectra present noticeable differences in the energy range up to 50 eV from the threshold. In particular, the edge intensity is lowered in the spectrum containing only the first shell water molecules, which exhibits a different shape in the region around the first minimum. The two spectra become identical for energy values higher than 60 eV, and this finding underlines the insensitivity of the EXAFS technique toward second shell contributions.

To assess the reliability of our results it is necessary to compare the total averaged XANES spectra with the experimental data. To this end all inelastic processes have been accounted for by convoluting the theoretical averaged spectra with a broadening Lorentzian function (see equation 2.8), and the corresponding E_s and A non-structural parameters (see section 2.3) have been optimized (see Table6.2). In the upper panel of Figure 6.5, the experimental XANES data of the Yb(III) ion in water are compared with the averaged theoretical spectrum including the first-shell clusters as derived from MD simulations. The overall agreement of the two spectra is not perfect in the entire energy range. In the lower panel Figure 6.5, the averaged theoretical spectrum including both the first and second hydration shells is compared with the experimental data. In this case, the agreement between the experimental and theoretical spectra is very good, the intensity of the white line is recovered and the shape of the first minimum region is very similar to the experimental data. It is important to remark that all the XANES

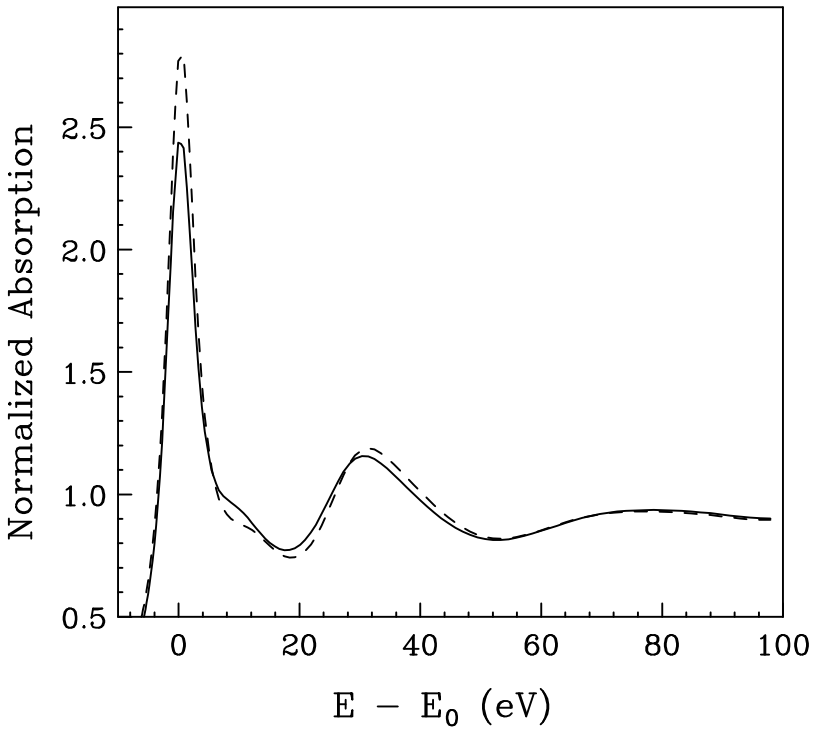

Figure 6.4: Comparison of the L_3-edge theoretical XANES spectrum obtained from the MD average including only the first hydration shell (solid line) and the averaged theoretical XANES spectrum including both the first and second shells (dashed line).

spectra have been calculated using the structural information obtained from the MD simulations without carrying out any minimization in the structural parameter space. Because of the high sensitivity of the XANES technique toward the structural environment of the photoabsorber this approach is a very strict test on the quality of the potentials used in the MD simulations, and the almost perfect agreement between the averaged theoretical and experimental XANES spectra proves the reliability of the entire computational procedure.

A complete picture of the potentiality of the XANES technique for the structural characterization of lanthanoid solutions has been obtained by analyzing the L_3-edge XANES spectra of two additional ions, namely, Nd(III) and Gd(III). The analysis of the aqueous solution XANES spectra has been carried out along the line of the Yb(III) ion. Figure 6.6 shows the comparison between the averaged theoretical spectra computed on the basis of the MD trajectories and the experimental data. The analysis including only the first hydration shells is reported in the upper panels while the averaged theoretical spectra computed including all the water molecules up to 6 Å are shown in the lower panels. Note that for both ions the agreement between the experimental and theoretical data improves when the second hydration shell is taken into account. Also in this case the inclusion of the higher distance ligands produces additional features that are clearly detectable in the

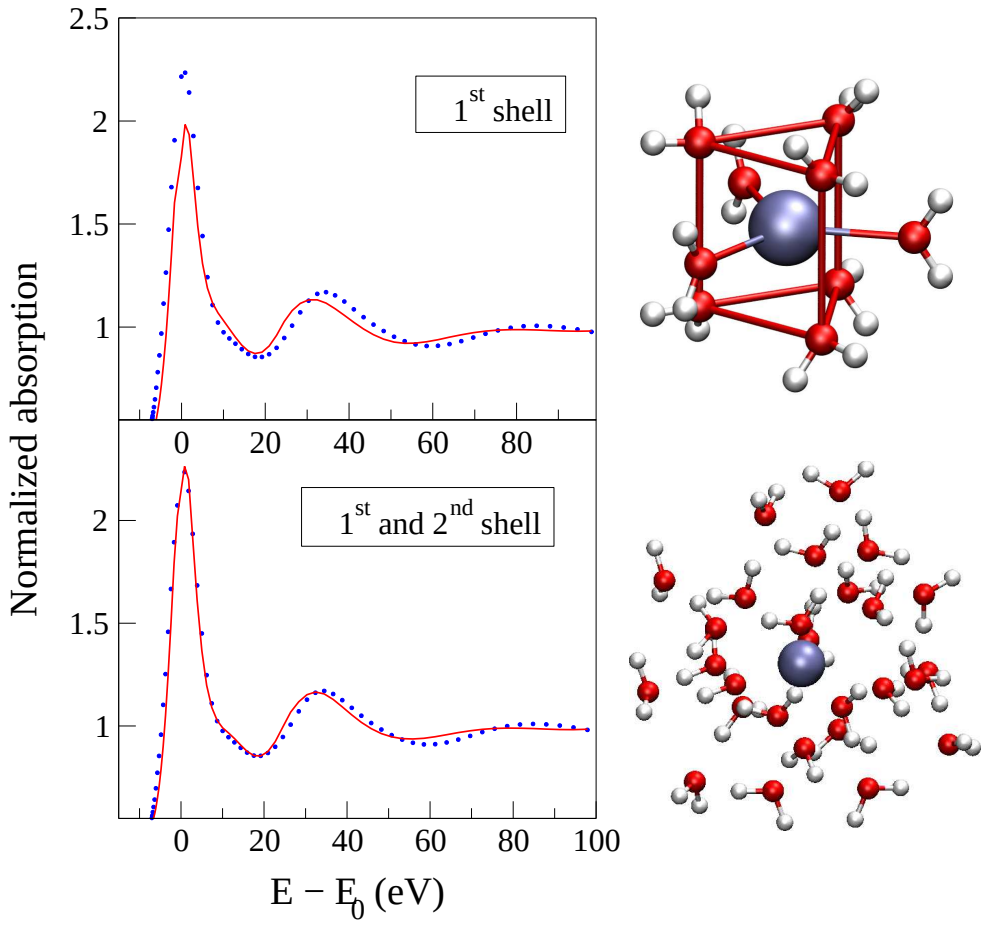

Figure 6.5: Upper panel: Comparison between the L_3-edge XANES experimental spectrum of Yb(III) aqueous solution (dotted blue line) and the MD averaged theoretical spectrum including only the first coordination sphere (solid red line). Lower panel: Comparison between the L_3-edge XANES experimental spectrum of the Yb(III) ion in aqueous solution (dotted blue line) and the MD averaged theoretical spectrum including both the first and second coordination shell (solid red line).

experimental data.

Finally, we have used the instantaneous configurations of the MD simulations to compute K-edge averaged XANES spectra for the three ions. In this case we have included only the first shell water molecules, and the comparison with the deconvolved experimental spectra is shown in Figure 6.7. The agreement between the experimental and theoretical spectra is quite good for all the three ions, proving simultaneously the reliability of the procedure and the insensitivity of the K-edge XANES spectra toward higher distance coordination shells.

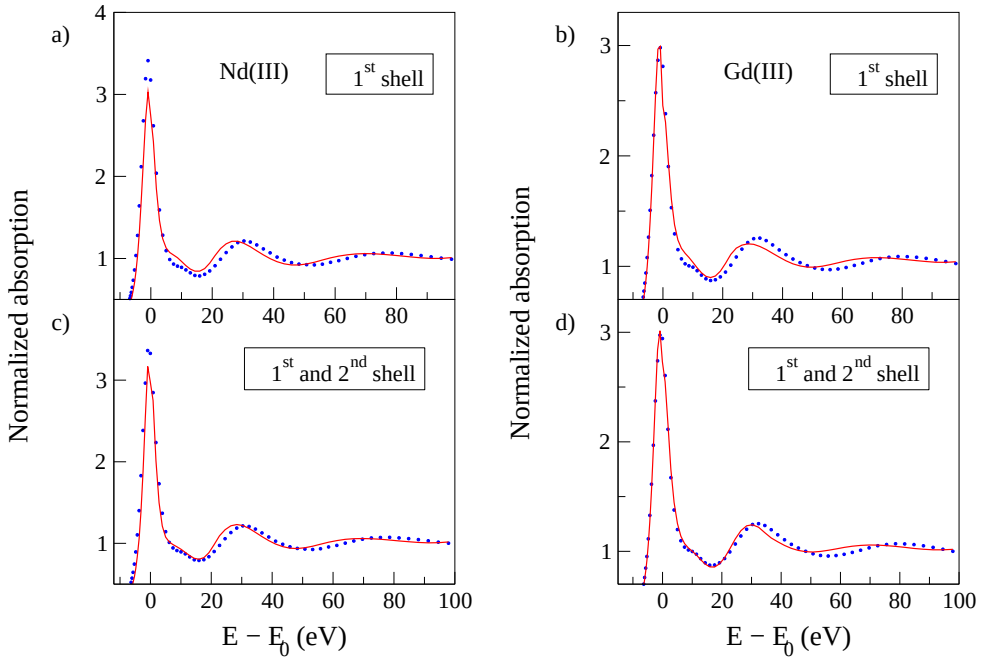

Figure 6.6: a) Comparison between the L_3-edge XANES experimental spectrum of the Nd(III) ion in aqueous solution (dotted blue line) and the MD averaged theoretical spectrum including only the first hydration sphere (solid red line); b) Comparison between the L_3-edge XANES experimental spectrum of the Gd(III) ion in aqueous solution (dotted blue line) and the MD averaged theoretical spectrum including only the first hydration sphere (solid red line); c) Comparison between the L_3-edge XANES experimental spectrum of the Nd(III) ion in aqueous solution (dotted blue line) and the MD averaged theoretical spectrum including both the first and second hydration shells (solid red line); d) Comparison between the L_3-edge XANES experimental spectrum of the Gd(III) ion in aqueous solution (dotted blue line) and the MD averaged theoretical spectrum including both the first and second hydration shells (solid red line).

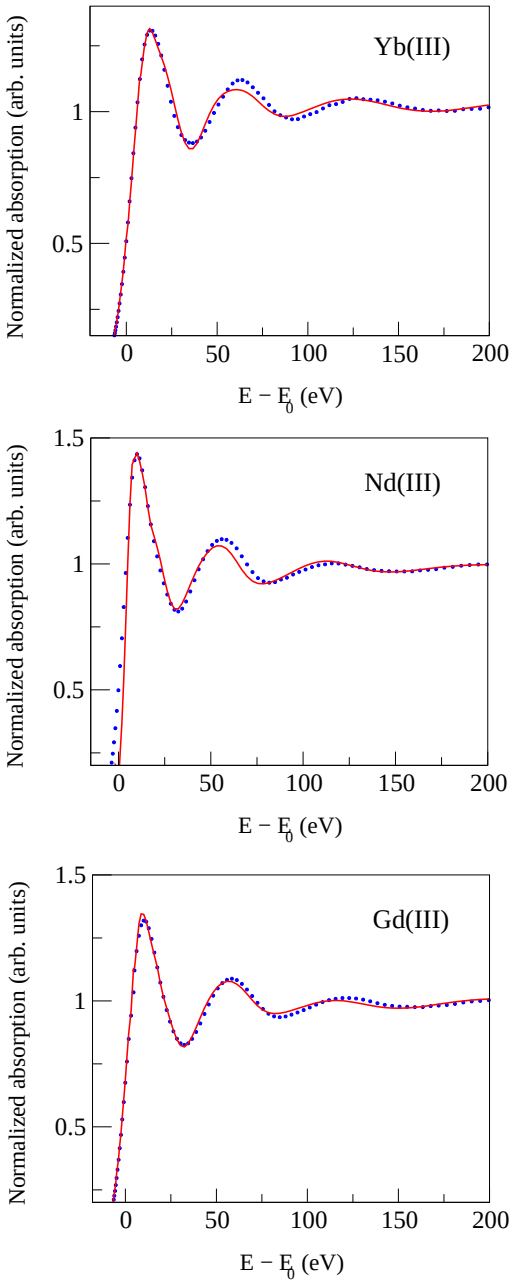

Figure 6.7: Comparison between the deconvolved K-edge XANES experimental spectra of the Yb(III), Nd(III), and Gd(III) ions in aqueous solution (dotted blue line) and the MD averaged theoretical spectra including only the first hydration shell (solid red line).

Table 6.2: Non-structural parameters as determined by MXAN from MD simulations. E_F (eV) is the Fermi energy level, E_s (eV) is the plasmon energy, A_s is the plasmon amplitude, E_0 (eV) is the threshold energy, and Γ_{exp} (eV) is the experimental resolution.

L_3-edge data					K-edge deconvolved data				
E_F	E_s	A_s	E_0	Γ_{exp}	E_F	E_s	A_s	E_0	Γ_{exp}
Nd(III)/water (from MD with first shell only)									
-7.9	14.3	2.3	0.7	6.5	-7.3	8.7	5.6	2.2	2.9
Nd(III) water (from MD with first and second shell)									
-9.0	14.6	3.6	0.7	2.2					
Gd(III)/water (from MD with first shell only)									
-8.6	15.4	5.4	1.2	4.3	-14.9	5.3	6.0	2.4	1.9
Gd(III) water (from MD with first and second shell)									
-10.0	25.0	6.6	1.6	2.3					
Yb(III)/water (from MD with first shell only)									
-7.7	18.0	3.8	1.6	4.2	-14.0	10.7	2.0	8.1	4.2
Yb(III) water (from MD with first and second shell)									
-9.1	16.8	4.0	1.6	1.2					

Chapter 7

Polarized Simulation Results

7.1 Combined EXAFS and MD simulation analysis

Recently Duvail et all. carried out polarized MD simulations of lanthanoid ions in aqueous solution in which the Ln-O interaction potentials have been built up on the basis of Shannon ionic radius of each element (see section 4.3). That ionic radii, in solid phase, reported by Shannon are a function of the number of oxygen atoms around the lanthanoid. As reference was taken the La(III) ionic radius corresponding to a ninefold structure, i.e., 1.216 Å, and for the other lanthanoids was taken the ninefold values for the lighter ones and both ninefold and eightfold values for heavier atoms. Thus we have for each Ln(III) heavier than Pm(III) a double set of simulations.
Figure 7.1 shows the Ln-O bond distances obtained from the MD simulations in comparison with the EXAFS results of a previous investigation [15]. All the structural results are collected in Table 7.1. For the largest ions, Ln=La-Pr, the MD Ln-O bond distances are shorter than the EXAFS results, while from Nd(III) to Gd(III) the MD and EXAFS structural parameters are, within estimated limits of error, in good agreement. Starting at Tb(III) up to Yb(III), the EXAFS bond distances place between the MD results for a nine and an eight coordination geometry, while for Lu(III) the EXAFS and MD simulation results for an eight coordination arrangement agree. On the basis of these results, we propose a new set of lanthanoids ionic radii in water (see Table 7.2) as the Shannon ionic radius plus an additional term given by the difference between EXAFS and MD simulation Ln-O bond distances:

$$Radius_{new} = Radius_{Shannon} + [(Ln - O_{EXAFS}) - (Ln - O_{MD})] \qquad (7.1)$$

In Figure 7.2 the new ionic radii, togheter with the Shannon ionic radii, for all the lanthanoid series are plotted. The use of the new set of ionic radii allowed to obtain MD simulations Ln-O bond distances that are in a very good agreement with the EXAFS results, as shown in Figure 7.3 and reported in Table 7.1.

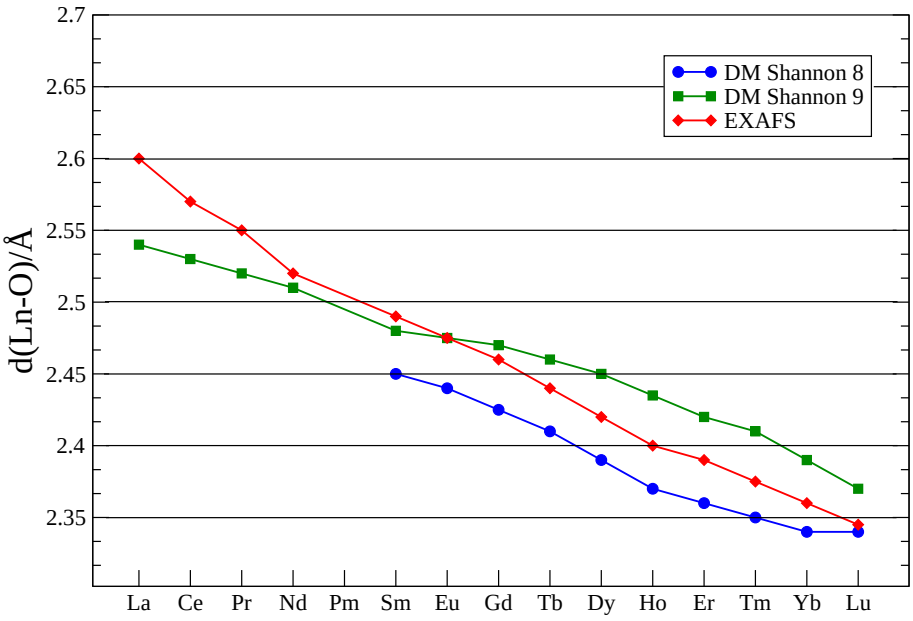

Figure 7.1: Ln-O bond distances obtained from the MD simulation using a ninefold values of the Shannon ionic radius (green squares) and an eightfold values of the Shannon ionic radius (blue circles), while the Ln-O mean bond distances obtained from EXAFS [15] are marked with red diamonds.

As previously done in section 6.2 a direct comparison between MD and EXAFS results can be performed by calculating the $\chi(k)$ theoretical signal associated with the MD Ln-O and Ln-H g(r)'s and by comparing it with the experimental spectrum, without carrying out any minimization procedure. For this analysis we selected four ions, Pr(III), Eu(III), Er(III) and Lu(III) as representative of the structural changes along the series. In Figure 7.4 the comparison between the EXAFS experimental signal and the total theoretical curves calculated using the MD g(r)'s is reported for Pr(III). In the upper section of the figure is shown the comparison between the total theoretical signal obtained from the MD g(r)'s using the Shannon ionic radius for a ninefold coordination (SIR-9) with the experimental spectrum, while in the lower section is reported the same comparison but with a total theoretical signal obtained from the MD g(r)'s using our new ionic radius (NRI). It is clear that the use of the new ionic radii leads to a substantial improvement in the agreement between theoretical and experimental data. In the case of Eu(III) the better agreement between the EXAFS experimental and theoretical spectra is for a nine coordinated structure using a Shannon ionic radii, that in this case coincides with the radius proposed by us (Figure 7.5), while for Er(III) the best agreement is with the use of our new ionic radius (Figure

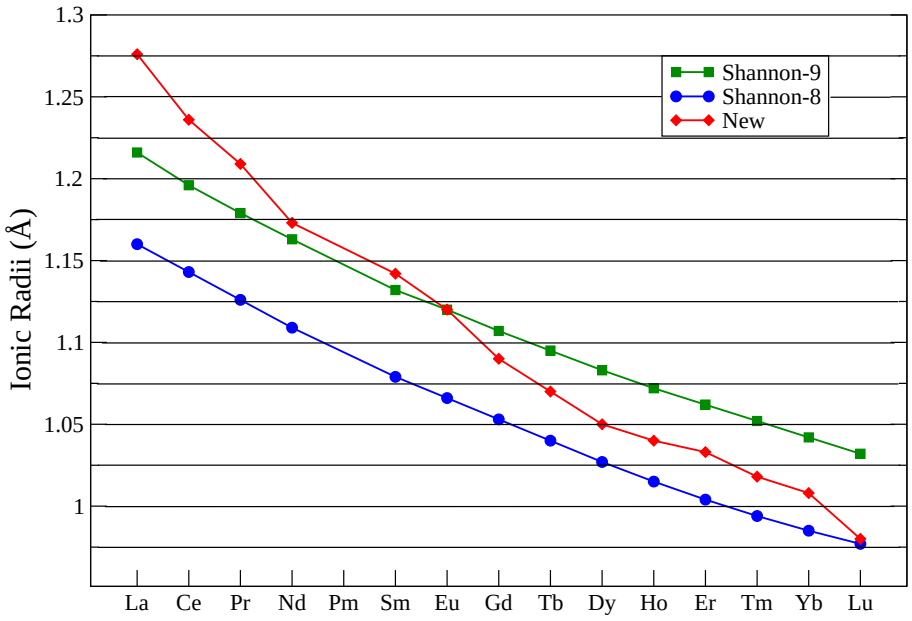

Figure 7.2: Ionic radii of the lanthanoid series in water solution as given by Shannon for a ninefold structure (green squares), an eightfold strucure (blue circles) and the new set of ionic radii as determined by the EXAFS and MD polarized simulations (red diamonds)

7.6). For the last element of the lanthanoid series, namely the Lu(III), the EXAFS experimental data are well reproduced with a MD simulation using a Shannon ionic radius corresponding to an eightfold structure (Figure 7.7).

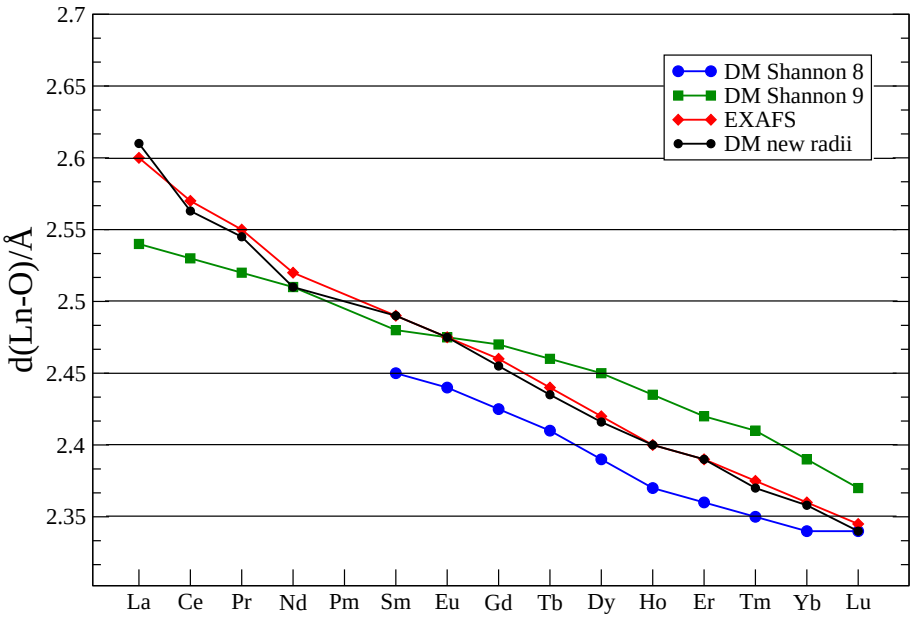

Figure 7.3: A summary of the results given in Table 7.1 of the lanthanoid(III) ions in aqueous solution as determined by EXAFS [15] and polarized MD simulations. The Ln-O bond distances obtained from the MD simulation using a ninefold values of the Shannon ionic radius and an eightfold values of the Shannon ionic radius are marked with green squares and blue circles respectively, the Ln-O mean bond distances obtained from EXAFS are marked with red diamonds, while the Ln-O bond distances obtained from the MD simulations using the new set of ionic radii are marked with black circles.

Table 7.1: Ln-O bond distances obtained from EXAFS [15], from the MD simulation using an eightfold values of the Shannon ionic radius (MD-8), from the MD simulation using a ninefold values of the Shannon ionic radius (MD-9) and from MD simulations using the new set of ionic radii.

	EXAFS	MD-8	MD-9	MD-new
La	2.600	-	2.540	2.610
Ce	2.570	-	2.530	2.563
Pr	2.550	-	2.520	2.545
Nd	2.520	-	2.510	2.510
Sm	2.490	2.450	2.480	2.490
Eu	2.475	2.440	2.475	2.475
Gd	2.460	2.425	2.470	2.455
Tb	2.440	2.410	2.460	2.435
Dy	2.420	2.390	2.450	2.416
Ho	2.400	2.370	2.435	2.400
Er	2.390	2.360	2.420	2.390
Tm	2.375	2.350	2.410	2.370
Yb	2.360	2.340	2.390	2.358
Lu	2.345	2.340	2.370	2.340

Table 7.2: Lanthanoids ionic radii in aqueous solution as determined by Shannon for an eightfold srtucture (RIS-8), a ninefold structure (RIS-9) and the new set of ionic radii determined by a combined EXAFS and polarized molecular dynamic simulations study.

	RIS-8	RIS-9	R-new
La	1.160	1.216	1.276
Ce	1.143	1.196	1.236
Pr	1.126	1.179	1.209
Nd	1.109	1.163	1.173
Sm	1.079	1.132	1.142
Eu	1.066	1.120	1.120
Gd	1.053	1.107	1.090
Tb	1.040	1.095	1.070
Dy	1.027	1.083	1.050
Ho	1.015	1.072	1.040
Er	1.004	1.062	1.033
Tm	0.994	1.052	1.018
Yb	0.985	1.042	1.008
Lu	0.977	1.032	0.980

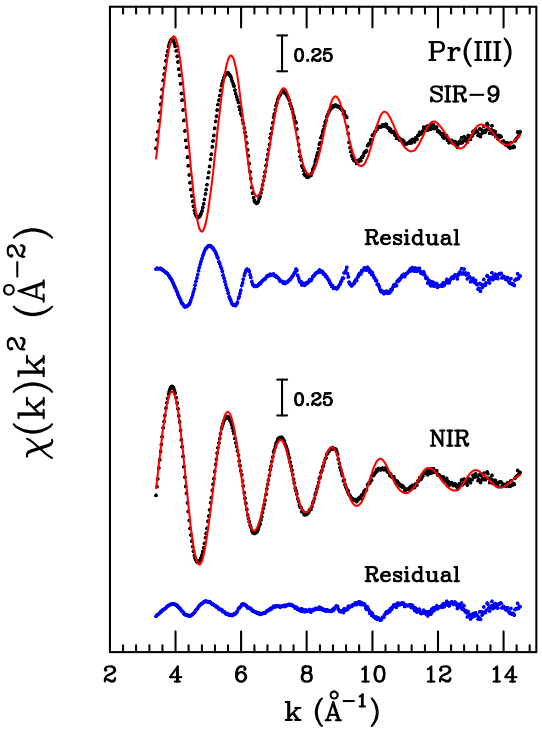

Figure 7.4: Analysis of the K-edge EXAFS spectra of aqueous solution of Pr(III) starting from the Ln-O and Ln-H radial distribution functions obtained from MD polarized simulations. From the top to the bottom of the panel the following curves are reported: the total theoretical signals (red lines) compared with the experimental spectrum (black dotted line) and the residual curves (blue dotted line) related to the use of a Shannon ionic radius for a ninefold coordination (SIR-9) and the use of the new ionic radius (NIR).

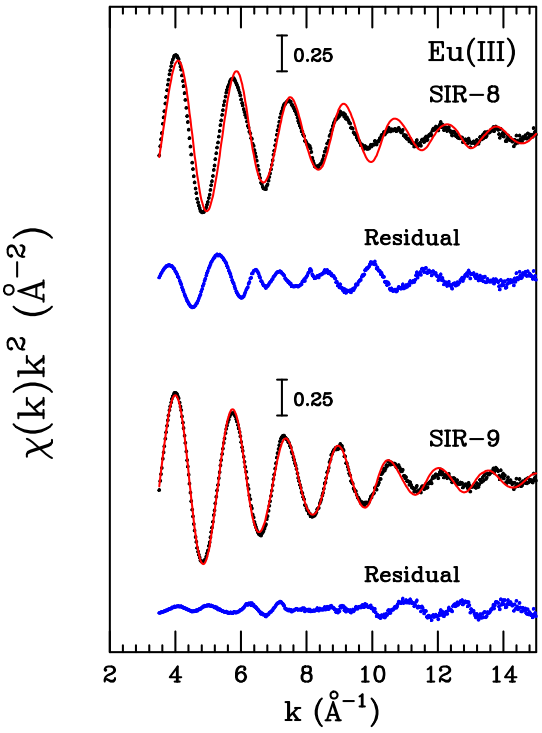

Figure 7.5: Analysis of the K-edge EXAFS spectra of aqueous solution of Eu(III) starting from the Ln-O and Ln-H radial distribution functions obtained from MD polarized simulations. From the top to the bottom of the panel the following curves are reported: the total theoretical signals (red lines) compared with the experimental spectrum (black dotted line) and the residual curves (blue dotted line) related to the use of a Shannon ionic radius for a ninefold coordination (SIR-9) and an eightfold coordination (SIR-8).

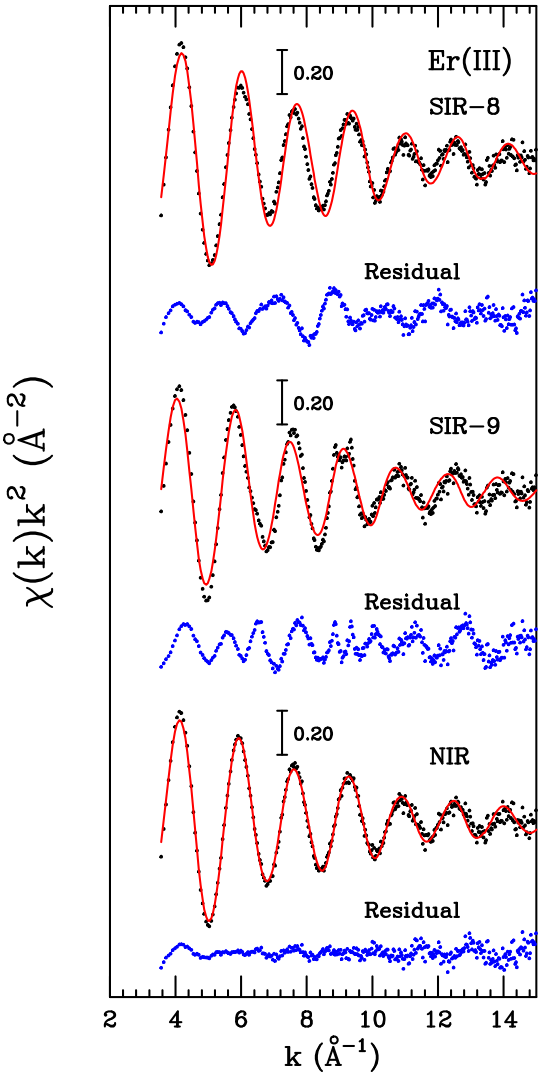

Figure 7.6: Analysis of the K-edge EXAFS spectra of aqueous solution of Er(III) starting from the Ln-O and Ln-H radial distribution functions obtained from MD polarized simulations. From the top to the bottom of the panel the following curves are reported: the total theoretical signals (red lines) compared with the experimental spectrum (black dotted line) and the residual curves (blue dotted line) related to the use of a Shannon ionic radius for a ninefold coordination (SIR-9), an eightfold coordination (SIR-8) and the new ionic radius (NIR).

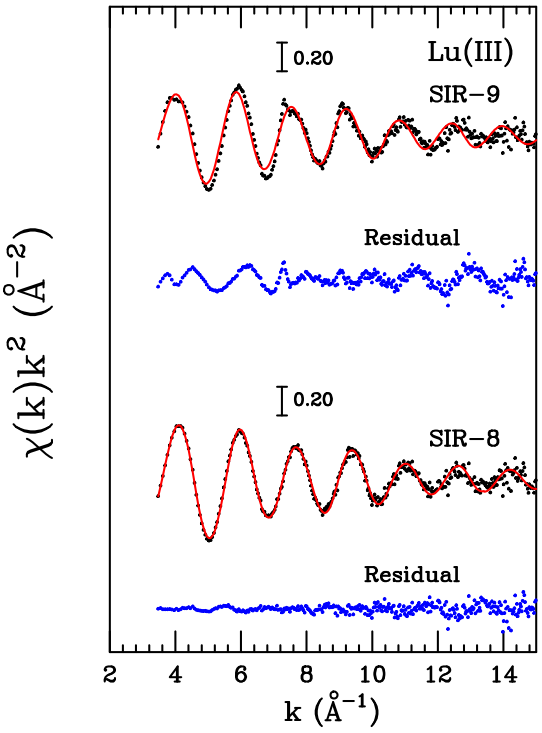

Figure 7.7: Analysis of the K-edge EXAFS spectra of aqueous solution of Lu(III) starting from the Ln-O and Ln-H radial distribution functions obtained from MD polarized simulations. From the top to the bottom of the panel the following curves are reported: the total theoretical signals (red lines) compared with the experimental spectrum (black dotted line) and the residual curves (blue dotted line) related to the use of a Shannon ionic radius for a ninefold coordination (SIR-9) and an eightfold coordination (SIR-8).

Chapter 8

Summary and conclusions

Previous experimental and theoretical works have shown that the hydration properties of the lanthanoid(III) ions are not so well established as assumed in the past years.[14, 16, 17, 15] In this paper, we have carried out a quantitative analysis of the K- and L_3-edge XANES spectra of Ln(III) ions in aqueous solution which was able to catch crucial structural properties of the hydration complexes along the lanthanoid series. The XANES spectroscopy has been found to be a very effective probe of the geometric structure of lanthanoid hydration clusters both in solid crystals and in aqueous solution. Across the series we observed a reduction of the coordination number, in the form of a progressive mean departure of a water molecule from the capping sites of the TTP prism, in agreement with the overall picture recently proposed on the basis of EXAFS results.[15] Changing the atom along the series one of the capping water molecules is less and less strongly bound to the Ln(III) ion, finally leaving the hydration complex. This gives rise to an eight-coordinated distorted bicapped trigonal prism with two different Ln-O capping distances for the last members of the series, as also observed for the hydrated scandium(III) ion.[33] It is important to stress that the XANES technique has allowed us to gain direct structural information on the exact geometry of the coordination polyhedron of the hydrated Ln(III) ions, that is achievable neither by EXAFS nor by crystallography. Due to different reasons both these techniques fail in providing an unambiguous high-temperature determination of the coordination geometry of the hydrated lanthanoid species. In the case of disordered systems the accuracy of the structural determination obtained by EXAFS can be inconclusive due to the well known limitations of this technique to determine coordination numbers and the geometry of polyhedral environments. Moreover, when dealing with distorted TTP complexes, the loosely bound atoms in the capping positions contribute less to the EXAFS signal, so that the bond-length determined by EXAFS is shorter than the true mean value. On the other hand, the crystallographic structures of Ln(III) hydrated trifluoromethanesulfonates at ambient temperature reveal that the occupancy of the capping sites decreases with increasing atomic number. When one of the capping molecules is absent, there is a displacement of the metal ion from the center of the prism towards the two remaining

capping waters which gives rise to distorted TTP geometries. This distortion is not detected by crystallography at room temperature as the high symmetry ($P6_3/m$) of the crystal structure is an average corresponding to a random orientation of the capping water molecules. Therefore, the capping bond distance obtained from x-ray diffraction is the mean value of two different sets of distances.

It is important to stress that the existence of distorted configurations of the the hydrated ion has been found in the low-temperature (100K) crystal structure of $[Lu(H_2O)_{8.2}](CF_3SO_3)_3$ and $[Sc(H_2O)_{8.0}](CF_3SO_3)_3$.[15, 33] As a result neither the EXAFS nor the crystallographic technique alone are able to provide a true picture of the geometry of the hydrated lanthanoid ions, while a reliable description of the structural change along the series has been obtained from the comparison of the results obtained from the two techniques.[15]

An interesting issue which emerged from this study is the different results obtained from the analysis of the K- and L_3-edge XANES spectra. In all cases the K-edge XANES spectra have been found to be insensitive to the second coordination shell. This is due to the very short lifetime of the excited atomic state for absorption edges above 30 keV which gives rise to a strong damping and broadening of the signal. This affects in particular the high-frequency components of the measured signal and consequently reduces the sensitivity of the technique to the more distant coordination shells. Note that the K-edge XANES spectra of the aqueous solution samples and trifluoromethanesulfonate solid salts are always identical, thus proving on the one hand that the different second coordination shells are not probed, on the other that the coordination of the first hydration shell is equal in water and in the solid.

An additional conclusion can be drawn comparing the L_3-edge XANES spectra of the three metal ions in aqueous solution. In the case of the lutetium(III) ion the second hydration shell has been found to provide a negligible contribution to the XANES spectrum. On the contrary, the neodymium(III), gadolinium(III) and ytterbium(III) XANES spectra of the solution could not be reproduced using the well-established TTP first hydration shell only, thus showing the need of including additional shells in the calculation. This finding can be explained by the different ionic radii, and consequently ligand properties, of the three ions. With decreasing size of the Ln(III) ion the repulsion between the prism and capping water molecules increases giving rise to a progressive weakening of the interaction between the central metal and the outer water molecules. As a consequence the occupancy of the capping sites decreases along the series until on average almost one water molecule departs in the last members of the series. The inability of the ion to keep the capping water molecules bound is also responsible for a reduced ability to structure water. As a result the second hydration shell is more mobile with increasing ionic size, becoming hardly observable in the XANES spectra.

In conclusion, we show that XANES is a very profitable tool to gain direct structural information on the coordination geometry of metal complexes with low symmetry as the hydrated lanthanoid(III) ions, that is not achiev-

able by other experimental techniques. The results of this investigation pave the route for the use of XANES for structural investigations of solid and liquid systems of metal ions with low symmetry, such as the actinoid series [95] and a wide class of metal-containing proteins [96, 97, 98] .

Bibliography

[1] D.T. Richens
The chemistry of aqua ions John Wiley & S. (1997).

[2] H. Othaki, T. Radnai
Chem. Rev. **93**, 1157, (1993).

[3] H.S. Frank, W.Y. Wen
Discuss. Faraday Soc. **24**, 133, (1957).

[4] R.W. Gurney
Ionic processes in solution McGraw Hill, New York (1953).

[5] F.M. Floris, A. Tani
J. Phys. Chem. **115**, 4750, (2001).

[6] a) J. K. Marsh
J. Chem. Soc., 554, (1939).
b) A. W. R. Wylie
Aust. Chem. Inst. J. Proc. **17**, 377, (1950).
c) D. H Templeton, C. H. Dauben
J. Am. Chem. Soc. **76**, 5237, (1954).

[7] F. H. Spedding, M. J. Pikal, B. O. Ayers
J. Phys. Chem. **70**, 2440, (1966).

[8] F. H. Spedding, K. C. Jones
J. Phys. Chem. **70**, 2450, (1966).

[9] F. H. Spedding, M. J. Pikal
J. Phys. Chem. **70**, 2430, (1966).

[10] T. Yamaguchi, M. Nomura, H. Wakita, H. Ohtaki
J. Chem. Phys. **89**, 5153, (1988).

[11] C. Cossy, A. C. Barnes, J. E. Enderby
J. Chem. Phys. **90**, 3254, (1989).

[12] C. Cossy, L. Helm, D. H. Powell, A. E. Merbach
New J. Chem. **19**, 27, (1995).

[13] a) A.Habenschuss, F. H. Spedding
J. Chem. Phys. **70**, 3758, (1979). b) A.Habenschuss, F. H. Spedding
J. Chem. Phys. **73**, 442, (1980).

[14] L. Helm, A. Merbach
Eur. J. Solid State Inorg. Chem. **28**, 245, (1991).

[15] I. Persson, P. D'Angelo, S. De Panfilis, M. Sandström, L. Eriksson
Chem. Eur. J. **14**, 3056, (2008).

[16] M. Duvail, M. Souaille, R. Spezia, T. Cartailler, P. Vitorge
J. Chem. Phys. **127**, 034503/1, (2007).

[17] M. Duvail, R. Spezia, P. Vitorge
Chem. Phys. Chem. **9**, 693, (2008).

[18] W. Meier, P. Bopp, M. M.Probst, E. Spohr, J. L Lin
J. Phys. Chem. **94**, 4672, (1990).

[19] S. Galera, J. M. Lluch, A. Oliva, J. Bertran, F. Foglia, L. Helm, A. E. Merbach
J. Phys. Chem. **17**, 773, (1993).

[20] L. Helm, F. Foglia, T. Kowall, A. E. Merbach
J. Phys. Condens. Matter **6**, A137, (1994).

[21] a) T. Kowall, F. Foglia, L. Helm,A. E. Merbach
J. Phys. Chem. **99**, 13078, (1995). b) T. Kowall, F. Foglia, L. Helm,A. E. Merbach
J. Am. Chem. Soc. **117**, 3790, (1995).

[22] S. Chaussedent, A. Monteil
J. Chem. Phys. **105**, 6532, (1996).

[23] T. Kowall, F. Foglia, L. Helm,A. E. Merbach
Chem. Eur. J. **2**, 285, (1996).

[24] H. S. Kim
Chem. Phys. Lett. **330**, 570, (2000).

[25] A. Chaumont, G. Wipff
Inorg. Chem. **43**, 5891, (2004).

[26] T. Ikeda, M. Hirata, T. Kimura
J. Chem. Phys. **122**, 244507, (2005).

[27] C. Clavaguera, R. Pollet, J. M. Soudan, V. Brenner, J. P. Dognon
J. Phys. Chem. **109**, 7614, (2005).

[28] S. R Hughes, T.-N. Nguyen, J. A. Capobianco, G. H Peslherbe
Int. J. Mass. Spectrom. **241**, 283, (2005).

[29] C. Clavaguera, F. Calvo, J. P. Dognon
J. Chem. Phys. **124**, 074505/1, (2006).

[30] A. Ruas, P. Guilbaud, C.Den Auwer, C. Moulin, J. P. Simonin, P. Turq, P. Moisy
J. Phys. Chem. A **110**, 11770, (2006).

[31] A. Chatterjee, E. N. Maslen, K. J. Watson
Acta Crystallogr.B **44**, 381, (1988).

[32] C. O. P Santos, E. E. Castellano, L. C. Machado, G. Vicentini
Inorg. Chim. Acta **110**, 83, (1985).

[33] A. Abbasi, P. Lindqvist-Reis, L. Eriksson, D. Sandström, S. Liding, I. Persson, M. Sandström
Chem. Eur. J. **11**, 4065, (2005).

[34] M. Benfatto, S. Della Longa
J. Synchrotron Radiat. **8**, 1087, (2001).

[35] P. D'Angelo, M. Benfatto, S. Della Longa, N. V. Pavel
Phys. Rev. B **66**, 064209, (2002).

[36] G. Chillemi, G. Mancini, N. Sanna, V. Barone, S. Della Longa, M. Benfatto, N. V. Pavel, P. D'Angelo
J. Am. Chem. Soc **129**, 5430, (2007).

[37] P. D'Angelo, M. Benfatto
J. Phys. Chem. A **108**, 4505, (2004).

[38] P. Frank, M. Benfatto, R. Szilagyi, P. DAngelo, S. Della Longa, K. O. Hodgson
Inorg. Chem. **44**, 1922, (2005).

[39] P. D'Angelo, O. M. Roscioni, G. Chillemi, S. Della Longa, M. Benfatto
J. Am. Chem. Soc **128**, 1853, (2006).

[40] P. D'Angelo, V. Migliorati, G. Mancini, G. Chillemi
J. Phys. Chem. A **112**, 11833, (2008).

[41] P. D'Angelo, S. De Panfilis, A. Filipponi, I. Persson
Chem. Eur. J. **14**, 3045, (2008).

[42] J.J. Rehr, R.C. Albers
Rev. Mod. Phys. **72**, 621, (2000).

[43] D.E. Sayers, E.A. Stern, F.W. Lytle.
Phys. Rev. Lett. **27**, 1204, (1971).

[44] E.A. Stern, D.E. Sayers, F.W. Lytle.
Phys. Rev. B **11**, 4836 (1975).

[45] C.R. Natoli, M. Benfatto
J. Phys. (Paris) Colloq. **47**, C8-11, (1986).

[46] M. Benfatto, C.R. Natoli
J. Phys. (Paris) Colloq. **48**, C9-1077, (1987).

[47] L. Hedin, B.I. Lundqvist
J. Phys. C **4**, 2064, (1971).

[48] A. Filipponi, A. Di Cicco, C.R. Natoli
Phys. Rev. B **52**, 15122 (1995).

[49] T.A. Tyson, K.O. Hodgson, C.R. Natoli, M. Benfatto
Phys. Rev. B **46**, 5997 (1992).

[50] P. Durham, J.B. Pendry, C.H. Hodges
Comput. Phys. Commun. **25**, 193 (1982).

[51] A.Michalowicz
J. Phys. IV Coll. C2, 235 (1997).

[52] J.J. Rehr, R.C. Albers
Phys. Rev. B **41**, 8139, (1990).

[53] J.E. Muller, O. Jepsen, J.W. Wilkins
Solid State Commun. **42**, 365, (1982).

[54] M. Benfatto, S. Della Longa, C.R. Natoli
J. Synchrotron Radiat. **10**, 51, (2003).

[55] P. D'Angelo, M. Benfatto, S. Della Longa, N.V. Pavel
Phys. Rev. B: Condens. Matter Mater. Phys. **66**, 064209, (2002).

[56] S. Della Longa, A. Arcovito, M. Girasole, J.L. Hazemann, M. Benfatto
Phys. Rev. Lett. **87**, 155501, (2001).

[57] B. T. Thole
Chem. Phys. **59**, 341, (1981).

[58] M. Duvail, P. Vitorge, R. Spezia
J. Chem. Phys. **130**, 104501, (2009).

[59] M. P. Allen, D. Tildesley
Computer Simulations of Liquids Clarendon Press, Oxford (1987).

[60] D. van der Spoel, E. Lindahl, B. Hess, A.R. van Buuren, E. Apol, P.J. Meulenhoff, D.P. Tieleman T.M. Sijbers, K. A. Feenstra, R. van Drunen, H.J.C. Berendsen
Gromacs User Manual version 3.3 www.gromacs.org (2005).

[61] P.M. Morse
Phys. Rev. **34**, 57, (1929).

[62] L. Verlet
Phys. Rev. **34**, 1311, (1967).

[63] R.W. Hockney, S.P. Goel
J. Comp. Phys. **14**, 148, (1974).

[64] D. Frenkel, B. Smit
Understanding Molecular Simulations: From Algorithms to Applications Academic Press (2003).

[65] P.P. Ewald
Ann. Phys. **64**, 253, (1921).

[66] T. Darden, D. York, L. Pedersen
J. Chem. Phys. **98**, 10089, (1993).

[67] U. Essmann, L. Perera, M.L. Berkowitz, T. Darden, H. Lee, L.G. Pedersen
J. Chem. Phys. **103**, 8577, (1995).

[68] B. Hess, H. Bekker, H.J.C. Berendsen, J.G.E.M. Fraaije
J. Comp. Chem. **18**, 1463, (1997).

[69] J.P. Ryckaert, G. Ciccotti, H.J.C. Berendsen
J. Comp. Phys. **23**, 327, (1977).

[70] H.J.C. Berendsen, J.P.M. Postma, A. Di Nola, J.R. Haak
J. Chem. Phys. **81**, 3684, (1984).

[71] S. Nosé
Mol. Phys. **52**, 255, (1984).

[72] W.G. Hoover
Phys. Rev. A **31**, 1695, (1985).

[73] M. Parrinello, A. Rahman
J. Appl. Phys. **52**, 7182, (1981).

[74] S. Nosé, M. L. Klein
Mol. Phys. **50**, 1055, (1983).

[75] A. Filipponi, M. Borowski, D.T. Bowron, S. Ansell, S. De Panfilis, A. Di Cicco, J.P. Itie
Rev. Sci. Instrum. **71**, 2422, (2000).

[76] M. O. Krause, J. H. Oliver
J. Phys. Chem. Ref. Data **8**, 329, (1979).

[77] A. Filipponi
J. Phys. B: At. Mol. Opt. Phys. **33**, 2835, (2000).

[78] P. D'Angelo, V. Migliorati, G. Mancini, V. Barone, G. Chillemi
J. Chem. Phys. **128**, 84502, (2008).

[79] A. Kodre, J. Padežnik Gomilšek, A. Mihelič, I. Arčon
Radiat. Phys. Chem. **75**, 188, (2006).

[80] P. D'Angelo, V. Barone, G. Chillemi, N. Sanna, W. Meyer-Klauke, N.V. Pavel
J. Am. Chem. Soc. **124**, 1958, (2002).

[81] P. D'Angelo, A. Di Nola, A. Filipponi, N.V. Pavel, D. Roccatano
J. Chem. Phys. **100**, 985, (1994).

[82] A. Filipponi, A. Di Cicco
Phys. Rev. B, **52**, 15135, (1995).

[83] H.J.C. Berendsen, J.R. Grigera, T.P. Straatsma
J. Chem. Phys. **91**, 6269, (1987).

[84] H.J.C. Berendsen, J.P.M. Postma, A. Di Nola, J.R. Haak
J. Chem. Phys. **81**, 3684, (1984).

[85] H.J.C. Berendsen, D. van der Spoel, R. van Drunen
Comput. Phys. Commun. **91**, 43, (1995).

[86] G. Hummer, L.R. Pratt, A.E. Garcia
J. Phys. Chem. A **102**, 7885, (1998).

[87] W. L. Jorgensen, J. Chandrasekhar, J. D. Madura, R. W. Impey, and M. L. Klein
J. Chem. Phys. **79**, 926, (1973).

[88] R. D. Shannon
Acta Crystallogr., Sect. A: Cryst. Phys., Diffr., Theor. Gen. Crystallogr. **32**, 751, (1976).

[89] M. Souaille, H. Loirat, D. Borgis, and M.-P. Gaigeot
Comput. Phys. Commun. **180**, 276, (2009).

[90] M. Sprik
J. Phys. Chem. **95**, 2283, (1991).

[91] K. Hayakawa, K. Hatada, P. D'Angelo, S. Della Longa, C. R. Natoli, M. Benfatto
J. Am. Chem. Soc. **126**, 15618, (2004).

[92] P. D'Angelo, A. Lapi, V. Migliorati, A. Arcovito, M. Benfatto, O. M. Roscioni, W. Meyer-Klaucke, S. Della-Longa
Inorg. Chem. **47**, 9905, (2008).

[93] A. Chatterjee, E. N. Maslen, K. J. Watson
Acta Crystallogr. Sect. B **44**, 381, (1988).

[94] a) P.J. Merkling, A. Muñoz-Paez, J.M. Martinez, R.R. Pappalardo, E. Sanchez Marcos
Phys. Rev. B **64**, 092201/1, (2001). b) P.J. Merkling, A. Muñoz-Paez, E. Sanchez Marcos
J. Am. Chem. Soc. **124**, 10911, (2002). c) F. Carrera, F. Torrico, D. T. Richens, A. Muñoz-Paez, J.M. Martinez, R.R. Pappalardo, E. Sanchez Marcos
J. Phys. Chem. B. **111**, 8223, (2007).

[95] Z. Szabó, T. Toraishi, V. Vallet, I. Grenthe
Coordination Chemistry Reviews **250**, 784, (2006).

[96] J.D. Cook, J.E. Penner-Hahn, T.L Stemmler
Methods Cell. Biol. **90**, 199, (2008).

[97] R.W. Strange, M.C. Feiters
Curr. Opin. Struct. Biol. **18**, 609, (2008).

[98] P. D'Angelo, S. Della Longa, A. Arcovito, M. Anselmi, A. Di Nola, G. Chillemi
J. Am. Chem. Soc. **132**, 14901, (2010).

Publications

1. Measurement of x-ray multielectron photoexcitations at the I^- K edge
   P. D'Angelo, A. Zitolo, V. Migliorati, N.V. Pavel
   Phys. Rew. B , **78**, 144105, (2008).

2. Ion Hydration in high-density water
   V. Migliorati, G, Chillemi, G. Mancini, A. Zitolo, S. Tatoli, A. Filipponi, P. D'Angelo
   J. Phys.: Conf. Ser., **190**, 012057, (2009).

3. Structural Investigation of Lanthanoid Coordination: a Combined XANES and Molecular Dynamics Study
   P. D'Angelo, A. Zitolo, V. Migliorati, G. Mancini, I. Persson, G. Chillemi
   Inorg. Chem., **48**, 10239, (2009).

4. Analysis of the Detailed Configuration of Hydrated Lanthanoid(III) Ions in Aqueous Solution and Crystalline Salts by Using K- and L_3-Edge XANES Spectroscopy
   P. D'Angelo, A. Zitolo, V. Migliorati,I. Persson
   Chem. Eur. J., **16**, 684, (2010).

5. Fe-heme structure in Cu,Zn superoxide dismutase from Haemophilus ducreyi by X-ray Absorption Spectroscopy
   P. D'Angelo, A. Zitolo, F. Pacello, G. Mancini, O. Proux, J.L. Hazemann, A. Desideri, A. Battistoni
   Archives of Biochemistry and Biophysics, **498**, 43, (2010).

6. Cuprizone neurotoxicity, copper deficiency and neurodegeneration
   F. Benetti, M. Ventura, B. Salmini, S. Ceola, D. Carbonera, S. Mammib, A. Zitolo, P. D'Angelo, E. Urso, M. Maffia, B. Salvato, E. Spisni
   NeuroToxicology, **31**, 509, (2010).

7. X-ray absorption spectroscopy study of the solvation structure of zinc(II) in dimethyl sulfoxide solution
   A. Zitolo, P. D'Angelo
   Chem. Phys. Lett., **499**, 113, (2010).

Acknowledgments

It is a pleasure for me to thank those who made this thesis possible, from a personal and a professional point of view. The first person I wish to thank is Paola D'Angelo, who has been my supervisor since the beginning of my study. She provided me with many helpful suggestions, important advice and constant encouragement during the course of this work, teaching me all I know about my scientific knowledge, becoming a solid professional reference point and a real friend.

My special thank goes to my colleague and best friend Valentina Migliorati. I am sure it is impossible to find a person with which to establish a so strong working and character affinity like her. I have known Vale since the beginning of my academic path and we are still together. It means that I am simply lucky.

Special thanks are due to Prof. Nicolae Viorel Pavel for the chance to work with his group.

I am grateful to Riccardo Spezia, Giovanni Chillemi and Stefano della Longa for their support.

I also acknowledge Giordano Mancini, Claudia Leggio and my favourite students, now friends, Salvatore, Gianluca and Mirko.

Finally I want to thank my parents and my sister, which always believed in me.